GALERKIN BOUNDARY ELEMENTS FOR EXTERIOR STOKES FLOWS

J. D'Elía, L. Battaglia, A. Cardona, M. Storti and G. Franck

Centro Internacional de Métodos Computacionales en Ingeniería (CIMEC)
Instituto de Desarrollo Tecnológico para la Industria Química (INTEC), UNL-CONICET
Güemes 3450, 3000-Santa Fe, Argentina.
E-mail: (jdelia, acardona, mstorti)@intec.unl.edu.ar, lbattaglia@santafe-conicet.gob.ar,
gerardofranck@yahoo.com.ar, web page http://www.cimec.org.ar,

Abstract. An indirect boundary integral equation for steady Stokes flow around a rigid body in the three-dimensional space is proposed, and is numerically solved by using collocation and Galerkin weighting procedures. The resulting double surface integrals of the Galerkin technique that express the pairwise interaction among all boundary elements, which are quadruple integrals, are computed on flat simplex triangles using a regularized quadrature scheme. Numerical examples include the steady creeping flow around the sphere of unit radius and the cube of unit edge length, covering issues on the convergence under mesh refinement and stability under small mesh perturbations.

1 INTRODUCTION

Integral equations frequently lead to boundary integral equations (BIEs) that are typically numerically solved by the boundary element method (BEM) using collocation or Galerkin weighting techniques (Hackbusch, 1995; Pozrikidis, 1996).

As it is well known, a standard discretization procedure of a BIE consists of three parts (Stenroos and Haueisen, 2008): tessellation of the boundary surfaces, approximation of the solution field with a linear combination of polynomial basis functions, and minimization of the error of the approximate solution with respect to some weighting functions. A simple tessellation of the boundary surface can be performed with flat simplex triangles, panels or elements, where their vertices are also the nodes of the boundary mesh. The basis functions are defined either on the elements, the nodes or the edges of the boundary mesh. In the first case, the basis functions are piecewise constant, i.e. each basis function has the value 1 on one panel and 0 elsewhere, and thus the number of basis functions corresponds to the number of elements in the surface tessellation. In the second case, the basis functions are piecewise linear, i.e. each basis function has the value 1 on one node and falls linearly to 0 toward the first-layer of neighboring nodes. In the third case, the basis functions are also piecewise linear, i.e. each basis function has the value 1 on one edge and falls linearly to 0 toward the first-layer of neighboring edges, e.g. those that are used in computational electromagnetism (Stenroos and Haueisen, 2008).

In general, the solution field cannot be accurately represented with a finite set of predefined basis functions, leading to an error that is minimezed with respect to a set of linearly independent weighting functions. The number of weighting functions is generally chosen to be the same as the number M of basis functions and, therefore, giving a system of M linear equations with M unknowns. On one side, a point collocation technique minimizes the residual in a discrete set of points defined with the Dirac function $\delta(\mathbf{x})$ that, typically, consists of the centroids of the elements in case of constant basis functions. Then, there are only single surface integrations, although these generate a non-symmetric system of algebraic equations. On the other side, a Galerkin weighting technique minimizes the residual over the whole surface instead of a discrete number of points, where the weighting functions are chosen identical to the basis functions. It leads to a symmetric system of algebraic equations, albeit it involves double surface integrations.

Examples of weighted alternatives in a BIE include the variational boundary element method (VBEM Alia et al. (2006)), the symmetric boundary element method (SBEM Frangi and Bonnet (1998); Vodicka et al. (2006)), or the (symmetric) Galerkin boundary element method (SGBEM or GBEM, respectively (Bonnet et al., 1998; Sutradhar et al., 2008)), as used, for example, in microflows (Schindler, 2006), elasticity (Mazza et al., 2008), fluid-structure interaction (Paquay, 2002) or acoustics (Schuhmacher, 2000). Fast integration in collocation techniques was used, for instance, in Fachinotti et al. (2007), where the self–integrals that contain singular kernels were analytically computed over linear triangles. Analytic expressions for surface potentials using isoparametric piecewise linear shape functions over flat triangles were developed in Fata (2009), whereas non-linear transformations for nearly singular integrals over planar triangles were used in collocation techniques in Scuderi (2008). Closed forms derived from a side local frame strategy are also commonly employed (Medina and Liggett, 1988; D'Elía et al., 2000a,b), where the surface integral over each panel is replaced by its closed contour integration, and a side local frame is used for each side contribution.

When either a VBEM, SBEM, SGBEM or a GBEM is used in the three-dimensional (3D) real space, it leads to compute double surface integrals, i.e. quadruple integrals, that account

for the pairwise interaction among all the panels of the surface mesh, a task that is carried out through a doubly nested loop $p, q = 1, 2, ..., E$, where E is the number of elements on the boundary mesh. The generic pair of interacting triangles is the support of the double surface integral, and the integral value represents the interaction coefficient between pairs of triangles, whose multiplicative kernel is obtained as the product of both panel kernels. In the case of kernels with a weak singularity there are analytical expressions of the double surface integrals in rather restricted cases, for instance, the "potential integrals" and self–integrals for flat triangles with a constant or linear numerator kernel (Eibert and Hansen, 1995; Sievers et al., 2005), and self–integrals for flat rectangles with a constant numerator kernel (López-Peña and Mosig, 2009). If two interacting triangles are not contiguous nor coincident, the multiplicative kernel is regular and a Gauss–Legendre quadrature formula can be used. However, when these triangles have a common edge or a common vertex, there are edge and vertex singularities, respectively. In the case of self–integrals, when both facets are coincident, the whole integration domain is weakly singular. For these reasons, special methods for the numerical integration are proposed in the literature, e.g. the edge singularity case in collocation techniques (Burghignoli et al., 2004). D. J. Taylor (2003) developed a systematic way for handling double surface integrals over flat triangular elements, based on a convenient reordering of the four iterate integrations that moves the weak singularity to the origin of the four-dimensional Euclidean real space (4D). Then, the Duffy transformation (Duffy, 1982) systematically was used which regularizes the integrand by using polar coordinates. Thus, Taylor chose a Gauss–Legendre numerical quadrature on three coordinates and performed an analytic integration in the fourth one. A slightly modified implementation of the Taylor scheme was presented in D'Elía et al. (2009a), where a full numerical quadrature was employed in the four integration coordinates in order to handle generic Green functions with a weak singularity.

Many boundary integral equations are of Fredholm type of first or second kind and are obtained through direct and indirect integral formulations (Beer and Watson, 1992). Indirect formulations in the case of creeping (or Stokes) flows (Power and Wrobel, 1995; D'Elía et al., 2009b) are commonly related to hydrodynamic double- and single-layer potentials (Ladyzhenskaya, 1969), where the interaction coefficient among points has a tensorial character and can be either a real or a complex value, corresponding to steady and harmonic Stokes flow, respectively. Examples of creeping flows around bodies are found, among other applications, in micro-electro-mechanical systems (MEMS) Wang (2002); Méndez et al. (2008); Berli and Cardona (2009). When a body has geometric discontinuities on its surface, such as corners and edges, there is a singular behavior of the stress and traction fields in both hydrodynamic and elasticity problems (Kozlov et al., 2001; Dimitrov et al., 2001). Nevertheless, it has already been shown that both boundary integral equations (Mustakis and Kim, 1998) and finite element (Dimitrov, 2004) techniques can be used for solving numerically these special cases.

In the present work, an indirect boundary integral equation of Fredholm type and second kind is proposed for the exterior steady creeping flow around a body in the three-dimensional space, and is numerically solved by using collocation and Galerkin weighting procedures. In the last case, a modified Taylor integration scheme is employed as a "black box" for the weakly singular double surface integrals among all the elements of the boundary mesh (Taylor, 2003; D'Elía et al., 2009a). Gauss-Legendre quadrature formulas using n_{1d} points in each integration coordinate, and flat simplex triangles are used in all cases. An isolated rigid body and an incompressible viscous fluid of Newtonian type are assumed. Numerical examples include the steady creeping flow around a unit radius sphere and a unit edge length cube, covering issues such as convergence of the numerical solution under mesh refinement and numerical stability

under mesh perturbations. In the case of the steady creeping flow around the unit cube, the traction coefficients close to the edges and corners are plotted for the flow eigenmodes considered by Mustakis and Kim (1998), in order to check the corresponding traction exponent laws against their semi-analytical computations. A comparison with a finite element computation is performed as well.

2 BOUNDARY INTEGRAL EQUATION WITH AN INDIRECT FORMULATION

2.1 Stokes equations for an exterior and steady creeping flow

The fluid velocity $v_i = v_i(\mathbf{x})$, with $i = 1, 2, 3$, and pressure $p = p(\mathbf{x})$ fields of a steady and creeping flow of an incompressible Newtonian viscous fluid, satisfy the Stokes equations (Power and Wrobel, 1995)

$$\mu \frac{\partial^2 v_i}{\partial x_j \partial x_j} = \frac{\partial p}{\partial x_i}$$
$$\frac{\partial v_i}{\partial x_i} = 0 \tag{1}$$

for all field points $\mathbf{x} = (x_1, x_2, x_3)$ in the exterior flow domain Ω^e to a closed surface A of arbitrary shape, where μ is the dynamic fluid viscosity. The boundary conditions include the non-slip boundary condition on the surface A given by

$$v_i(\mathbf{x}) + u_i(\mathbf{x}) = 0 \qquad \text{for all } \mathbf{x} \in A \tag{2}$$

where $u_i = u_i(\mathbf{x})$ is the prescribed velocity on the surface A, and the radiation conditions at infinity

$$v_i(\mathbf{x}) = O(1/R)$$
$$p(\mathbf{x}) = O(1/R^2) \tag{3}$$

as $R \to \infty$, where $R = \|\mathbf{x}\|_2$ is the Euclidean distance from the origin $O(x, y, z)$.

2.2 Classical hydrodynamic potentials

It is known that the velocity $v_i^{\mathrm{DL}}(\mathbf{x})$ and pressure $p^{\mathrm{DL}}(\mathbf{x})$ fields due to a hydrodynamic double-layer (DL) potential generated by a (surface) density layer $\boldsymbol{\psi}$ decrease as

$$v_i^{\mathrm{DL}}(\mathbf{x}; \boldsymbol{\psi}) = O(1/R^2)$$
$$p^{\mathrm{DL}}(\mathbf{x}; \boldsymbol{\psi}) = O(1/R^3) \tag{4}$$

as $R \to \infty$, and cannot exert net force nor torque on the surface A. Thus, since a double-layer potential $\boldsymbol{\psi}$ alone cannot reproduce an arbitrary regular Stokes flow in the exterior domain Ω^e, Odqvist (e.g. Power and Wrobel (1995); Power and Miranda (1987) and references therein) added an ad hoc combination of six single-layer potentials produced by (surface) density layers $\boldsymbol{\phi}$ to fix this shortcoming. The densities of these single-layer potentials are the eigenfunctions of the adjoint integral operator of the double-layer potential; although, in general, they are not explicitly known (Power and Miranda, 1987).

2.3 An extension of the completed double-layer boundary integral equation method

The "completed double-layer boundary integral equation method", as it is termed in the literature (e.g. Power and Wrobel (1995), Sec. 6.2, p. 196, or Kim and Karrila (1991)) completes the deficient range of the double-layer potential without recourse to the eigenfunctions of its adjoint

integral operator. This approach is an extension to the Stokes equation of the Mikhlin results of the exterior Dirichlet problem for the Laplace equation (e.g. Power and Wrobel (1995); Power and Miranda (1987) and references therein). It can be written as

$$v_i(\mathbf{x}) \equiv v_i(\mathbf{x}; \boldsymbol{\psi}, \boldsymbol{\alpha}, \boldsymbol{\beta}) = w_i^{\mathrm{DL}}(\mathbf{x}; \boldsymbol{\psi}) + v_{ik}(\mathbf{x})\alpha_k + r_{ik}(\mathbf{x})\beta_k \qquad \text{for all } \mathbf{x} \in \Omega^e \qquad (5)$$

where $w_i^{\mathrm{DL}}(\mathbf{x}; \boldsymbol{\psi})$ is the perturbation velocity due to a double-layer potential produced by a (surface) density layer $\boldsymbol{\psi}$, whereas

$$v_{ik}(\mathbf{x}) = -\frac{1}{8\pi\mu}\left[\frac{\delta_{ik}}{R} + \frac{x_i x_k}{R^3}\right] \qquad (6)$$

is a Stokeslet, i.e. the Green function of the non-homogeneous Stokes system given by Eq. (1), when the forcing term is the point force $\delta(\mathbf{x})\delta_{ik}$, located at the origin and with unit value only in the k-direction, and

$$r_{ik}(\mathbf{x}) = -\frac{1}{8\pi\mu}\frac{\epsilon_{ipq}\delta_{pk}x_q}{R^3} \qquad (7)$$

is a rotlet, i.e. the corresponding Green function when the forcing term is given by the point torque $\epsilon_{ipq}(\partial/\partial x_q)\delta_{pk}\delta(\mathbf{x})$, located at the origin, δ_{ik} is the Kronecker delta, which is 1 if $i = k$ and 0 otherwise, while ϵ_{ijk} is the third order permutation symbol whose components are defined to be +1 if (i, j, k) is an even permutation of (1,2,3), -1 if it is an odd permutation and 0 if any index is repeated. Thus, this formulation adds to the double-layer potential $w_i^{\mathrm{DL}}(\mathbf{x}; \boldsymbol{\psi})$ a Stokeslet of strength α_k and a rotlet of strength β_k, both located at the origin. On one side, the Stokeslet exerts a total force equal to its strength, and zero total torque on any closed surface enclosing it, whereas the rotlet exerts a total torque equal to its strength, and zero total force on any closed surface enclosing it. On the other side, the double-layer potential with a well-defined density layer $\boldsymbol{\psi}$ yields zero total force and torque on the closed surface A. Therefore, the total force and torque resulting from the flow field defined by Eq. (5) are equal to the strengths $\boldsymbol{\alpha}$ and $\boldsymbol{\beta}$, respectively. This extension was proposed by Power and Miranda (1987), and further details are given in Power and Wrobel (1995); Kim and Karrila (1991).

A drawback of this scheme is that the velocity field has the typical behaviour of a concentrated source, a Stokeslet and a rotlet in this case and, thus, the traction patterns close to the geometric discontinuities of the closed surface, such as corners and edges, are smeared. For this reason, in the present work, the velocity field $v_i(\mathbf{x})$ is thought of as a linear superposition between the velocity field produced by a double-layer potential $w_i^{\mathrm{DL}}(\mathbf{x}; \boldsymbol{\psi})$ plus a single-layer (SL) one $w_i^{\mathrm{SL}}(\mathbf{x}; \boldsymbol{\phi})$, i.e.

$$v_i(\mathbf{x}) \equiv v_i(\mathbf{x}; \boldsymbol{\psi}; \boldsymbol{\phi}) = w_i^{\mathrm{DL}}(\mathbf{x}; \boldsymbol{\psi}) + w_i^{\mathrm{SL}}(\mathbf{x}; \boldsymbol{\phi}) \qquad \text{for all } \mathbf{x} \in \Omega^e \qquad (8)$$

where the single-layer surface density $\boldsymbol{\phi}(\mathbf{y})$ is equivalent to a distributed system of point forces on the surface A that can exert a net torque and, thus, it makes unnecessary to introduce a surface density of rotlets.

2.4 Velocity potential of a double-layer surface density

The velocity potential due to a double-layer surface density $\boldsymbol{\psi}(\mathbf{y})$ is defined as (Power and Wrobel, 1995)

$$w_i^{\mathrm{DL}}(\mathbf{x}; \boldsymbol{\psi}) = \int_A \mathrm{d}A_{\mathbf{y}}\, K_{ij}(\mathbf{x}, \mathbf{y})\psi_j(\mathbf{y})$$

$$\text{with} \quad K_{ij}(\mathbf{x}, \mathbf{y}) = -\frac{3}{4\pi}\frac{r_i r_j r_k}{r^5}n_k(\mathbf{y}) \qquad (9)$$

where $dA_{\mathbf{y}} = dA(\mathbf{y})$ is the differential area, $\mathbf{y} = (y_1, y_2, y_3)$ is the source point, $\mathbf{r} = (r_1, r_2, r_3)$ is the relative position, with $\mathbf{r} = \mathbf{x} - \mathbf{y}$ and $r = \|\mathbf{r}\|_2$, while $\mathbf{n}(\mathbf{y})$ is the unit normal at $\mathbf{y}$. As it is well known in the Green function theory, as well as in solid and fluid mechanics, the j column of the tensor $K_{ij}(\mathbf{x}, \mathbf{y})$ physically represents the perturbation velocity induced by a double surface layer density of unit value on the j-component only. This kernel has the polarity $r^{-2+\lambda}$, where λ is the Lyapunov exponent of the surface, with $\lambda \in \mathbb{R}$ and $0 < \lambda \leq 1$. If the density $\psi_j(\mathbf{y})$ is smooth enough, it is known that the double-layer velocity $w_i^{\mathrm{DL}}(\mathbf{x}; \boldsymbol{\psi})$ verifies the jump property (e.g. Ladyzhenskaya (1969), Sec. 3.2, Eq. 22, p. 57),

$$\mathbf{w}^{\mathrm{DL}}(\mathbf{x}; \boldsymbol{\psi})_{(i)} - \mathbf{w}^{\mathrm{DL}}(\mathbf{x}; \boldsymbol{\psi})_{(e)} = \boldsymbol{\psi}(\mathbf{x}) \tag{10}$$

across the single closed surface A when $\mathbf{x} \in A$, where subscripts (i) and (e) denote the limiting values of $\mathbf{w}^{\mathrm{DL}}(\mathbf{x}; \boldsymbol{\psi})$ on the surface A, in case this surface is approached from inside or outside, respectively, and given by

$$
\begin{aligned}
w_i^{\mathrm{DL}}(\mathbf{x}; \boldsymbol{\psi})_{(i)} &= +\frac{1}{2}\psi_i(\mathbf{x}) + w_i^{\mathrm{DL}}(\mathbf{x}; \boldsymbol{\psi}) \\
w_i^{\mathrm{DL}}(\mathbf{x}; \boldsymbol{\psi})_{(e)} &= -\frac{1}{2}\psi_i(\mathbf{x}) + w_i^{\mathrm{DL}}(\mathbf{x}; \boldsymbol{\psi})
\end{aligned}
\tag{11}
$$

whereas

$$w_i^{\mathrm{DL}}(\mathbf{x}; \boldsymbol{\psi}) = \int_A dA_{\mathbf{y}}\, K_{ij}(\mathbf{x}, \mathbf{y})\psi_j(\mathbf{y}) \tag{12}$$

denotes the direct value of $w_i^{\mathrm{DL}}(\mathbf{x}; \boldsymbol{\psi})$ on the surface A. Moreover, on smooth surfaces (Kim and Karrila, 1991),

$$\int_A dA_{\mathbf{y}}\, K_{ij}(\mathbf{x}, \mathbf{y}) = \frac{1}{2}\delta_{ij} \tag{13}$$

2.5 Velocity potential of a single-layer surface density

The velocity potential of a single-layer surface density $\phi(\mathbf{y})$ is defined as (Power and Wrobel, 1995)

$$
\begin{aligned}
w_i^{\mathrm{SL}}(\mathbf{x}; \boldsymbol{\phi}) &= \int_A dA_{\mathbf{y}}\, \tilde{S}_{ij}(\mathbf{x}, \mathbf{y})\phi_j(\mathbf{y}) \\
\text{where} \quad \tilde{S}_{ij}(\mathbf{x}, \mathbf{y}) &= -\frac{1}{8\pi\mu}\left[\frac{\delta_{ij}}{r} + \frac{r_i r_j}{r^3}\right]
\end{aligned}
\tag{14}
$$

and it represents Stokeslet singularities, i.e. point forces distributed over the surface A. The kernel $\tilde{S}_{ij}(\mathbf{x}, \mathbf{y})$ is related to a point force located at the integration point $\mathbf{y}$ and oriented in the i direction, with polarity r^{-1}. The kernel can be obtained from the Kelvin one for elasticity in the incompressible case (Fachinotti et al., 2007), which means the Poisson ratio is $1/2$. If the density $\phi(\mathbf{y})$ is smooth enough, the single-layer $\mathbf{w}^{\mathrm{SL}}(\mathbf{x}; \boldsymbol{\phi})$ is continuous in the whole real space $\mathbb{R}^3$. Furthermore, when ϕ is bounded and integrable, then the function $\mathbf{w}^{\mathrm{SL}}(\mathbf{x}; \boldsymbol{\phi})$ is Hölder-continuous in the entire space, i.e.

$$\mathbf{w}^{\mathrm{SL}}(\mathbf{x}; \boldsymbol{\phi})_{(i)} = \mathbf{w}^{\mathrm{SL}}(\mathbf{x}; \boldsymbol{\phi})_{(e)} = \mathbf{w}^{\mathrm{SL}}(\mathbf{x}; \boldsymbol{\phi}) \tag{15}$$

2.6 An indirect BIE of Fredholm type and second kind with a combined surface density

In order to exclude the rigid body motions, following an idea introduced in Power and Miranda (1987) and extensively reviewed in Kim and Karrila (1991); Power and Wrobel (1995), it is convenient to choose the linear dependence

$$\phi_i(\mathbf{y}) = c\,\delta_{ij}\psi_j(\mathbf{y}) \qquad \text{with } c = \rho_1 U_1 \tag{16}$$

where ρ_1 and U_1 and are the unit fluid density and unit speed, respectively. The conversion factor c is introduced since both layer densities ϕ and ψ have different physical dimensions, that is, ϕ constitutes a force surface density (or pressure), e.g. N/m^2, while ψ is a perturbation velocity, e.g. ms^{-1}. Then,

$$\phi_j(\mathbf{y}) = c\,\psi_j(\mathbf{y}) \tag{17}$$

and the perturbation velocity due to a single-layer potential is rewritten as

$$w_i^{\mathrm{SL}}(\mathbf{x};\boldsymbol{\psi}) = \int_A \mathrm{d}A_{\mathbf{y}}\, S_{ij}(\mathbf{x},\mathbf{y})\psi_j(\mathbf{y}) \tag{18}$$

where now

$$S_{ij}(\mathbf{x},\mathbf{y}) = -\frac{U_1}{8\pi\nu_1}\left[\frac{\delta_{ij}}{r} + \frac{r_i r_j}{r^3}\right] \tag{19}$$

is the "kinematic" Stokeslet kernel, and $\nu_1 = \mu_1/\rho_1$ is the unit kinematic fluid viscosity. Then, the perturbation velocity from the exterior side of the surface A is given by Eq. (8)

$$v_i(\mathbf{x}) = w_i^{\mathrm{DL}}(\mathbf{x};\boldsymbol{\psi})_{(e)} + w_i^{\mathrm{SL}}(\mathbf{x};\boldsymbol{\psi})_{(e)} \qquad \text{for all } \mathbf{x} \in A \tag{20}$$

and taking into account the first boundary condition in Eq. (2),

$$w_i^{\mathrm{DL}}(\mathbf{x};\boldsymbol{\psi})_{(e)} + w_i^{\mathrm{SL}}(\mathbf{x};\boldsymbol{\psi})_{(e)} = -u_i(\mathbf{x}) \qquad \text{for all } \mathbf{x} \in A \tag{21}$$

Using the exterior limit case of Eq. (11) and replacing by Eq. (19), Eq. (21) gives

$$-\frac{1}{2}\psi_i(\mathbf{x}) - \int_A \mathrm{d}A_{\mathbf{y}}\,[K_{ij}(\mathbf{x},\mathbf{y}) - S_{ij}(\mathbf{x},\mathbf{y})]\,\psi_j(\mathbf{y}) = -u_i(\mathbf{x}) \qquad \text{for all } \mathbf{x} \in A \tag{22}$$

Taking into account Eq. (13), the first term on the left hand side of Eq. (22) is introduced inside the integral, and it results in the boundary integral equation

$$\int_A \mathrm{d}A_{\mathbf{y}}\,\{[S_{ij}(\mathbf{x},\mathbf{y}) - K_{ij}(\mathbf{x},\mathbf{y})]\,\psi_j(\mathbf{y}) + K_{ij}(\mathbf{x},\mathbf{y})\psi_j(\mathbf{x})\} = -u_i(\mathbf{x}) \qquad \text{for all } \mathbf{x} \in A \tag{23}$$

for the combined density $\boldsymbol{\psi}$, with $i,j = 1,2,3$. Using matrix notation, Eq. (23) is rewritten as

$$\mathbf{g}(\mathbf{x}) + \mathbf{u}(\mathbf{x}) = \mathbf{0} \qquad \text{for all } \mathbf{x} \in A \tag{24}$$

which is a boundary integral equation of Fredholm type and second kind, with source term $-\mathbf{u}(\mathbf{x})$, whereas

$$\mathbf{g}(\mathbf{x}) \equiv \int_A \mathrm{d}A_{\mathbf{y}}\,[\mathbf{H}(\mathbf{x},\mathbf{y})\boldsymbol{\psi}(\mathbf{y}) + \mathbf{K}(\mathbf{x},\mathbf{y})\boldsymbol{\psi}(\mathbf{x})] \qquad \text{for all } \mathbf{x} \in A \tag{25}$$
$$\text{with} \quad \mathbf{H}(\mathbf{x},\mathbf{y}) = \mathbf{S}(\mathbf{x},\mathbf{y}) - \mathbf{K}(\mathbf{x},\mathbf{y})$$

is a boundary integral operator with kernels $\mathbf{H}(\mathbf{x},\mathbf{y})$ and $\mathbf{K}(\mathbf{x},\mathbf{y})$. These kernels couple the double-layer surface density ψ at the integration point $\mathbf{y}$ and the field point $\mathbf{x}$.

3 NUMERICAL FORMULATIONS

Two numerical formulations are considered for solving the integral boundary equation given by Eq. (24). First, a collocation technique (Beer and Watson, 1992; Power and Wrobel, 1995) is employed and, next, a GBEM is used (Hackbusch, 1995). Numerical results were found using both methods. These techniques use a doubly nested loop over the panels $p, q = 1, 2, ..., E$, where the $\mathbf{x}$ and $\mathbf{y}$ points are related to the p, q panels, respectively, see Fig. 1. Element and nodal values are denoted with supra and sub indexes, respectively. Finally, a semi-analytic integration over triangles is summarized.
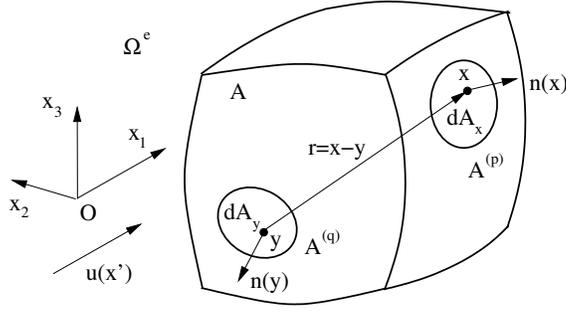
Figure 1: Sketch of a closed and piecewise smooth surface A with an exterior flow domain Ω^e: the field point $\mathbf{x}$, the source point $\mathbf{y}$, the relative position $\mathbf{r} = \mathbf{x} - \mathbf{y}$, the unit normals $\mathbf{n}(\mathbf{x}), \mathbf{n}(\mathbf{y})$, and the differential areas $\mathrm{d}A_\mathbf{x}$, $\mathrm{d}A_\mathbf{y}$.

3.1 Collocation using constant elements

Assuming that the density layer $\boldsymbol{\psi}(\mathbf{y})$ on the surface of each panel is constant, it can be extracted out of the surface integrals in Eq. (24) and using a standard collocation technique, it results in the system of equations

$$\sum_{q=1}^{E} \int_{A^{(q)}} \mathrm{d}A_\mathbf{y} \left[\mathbf{H}^{(p,q)}\boldsymbol{\psi}^{(q)} + \mathbf{K}^{(p,q)}\boldsymbol{\psi}^{(p)} \right] = -\mathbf{u}^{(p)} \tag{26}$$

where the elemental matrices $\mathbf{H}^{(p,q)} = \mathbf{H}(\mathbf{x}^{(p)}, \mathbf{x}^{(q)})$ and $\mathbf{K}^{(p,q)} = \mathbf{K}(\mathbf{x}^{(p)}, \mathbf{x}^{(q)})$, as well as the vectors $\mathbf{u}^{(p)} = \mathbf{u}(\mathbf{x}^{(p)})$ and $\boldsymbol{\psi}^{(p)} = \boldsymbol{\psi}(\mathbf{x}^{(p)})$, are evaluated at the panel centroids $\mathbf{x}^{(p)}$ for $p, q = 1, 2, ..., E$. Re-ordering

$$(\mathbf{F} + \mathbf{S})\boldsymbol{\Psi} = -\mathbf{U} \qquad \text{with } \boldsymbol{\Psi}, \mathbf{U} \in \mathbb{R}^{3E \times 1} \text{ and } \mathbf{F}, \mathbf{S} \in \mathbb{R}^{3E \times 3E} \tag{27}$$

where the global matrices are given by $\mathbf{F} = [\mathbf{F}^{(p,q)}]$ and $\mathbf{S} = [\mathbf{S}^{(p,q)}]$, while the global vectors are $\boldsymbol{\Psi} = [\boldsymbol{\psi}^{(p)}]$ and $\mathbf{U} = [\mathbf{u}^{(p)}]$. After simple algebra, the $\mathbf{F}$ matrix is given by

$$\mathbf{F}^{(p,q)} = \begin{cases} \displaystyle\sum_{e=1, e \neq p}^{E} \mathbf{K}^{(p,e)} & \text{when } q = p \\ -\mathbf{K}^{(p,q)} & \text{otherwise} \end{cases} \tag{28}$$

and $\mathbf{S}^{(p,q)} = \mathbf{S}(\mathbf{x}^{(p)}, \mathbf{x}^{(q)})$. It is known that the matrix system of Eq. (27) obtained with a collocation technique is regular and well conditioned (Hackbusch, 1995).

3.2 Galerkin weighting using linear elements

The fields $\boldsymbol{\psi}(\mathbf{x})$ and $\mathbf{u}(\mathbf{x})$ in Eq. (24) are approximated with $\hat{\boldsymbol{\psi}}(\mathbf{x})$ and $\hat{\mathbf{u}}(\mathbf{x})$ using linear elements. The standard Galerkin weighting technique chooses the nodal shape functions $\mathbf{N}_i(\mathbf{x})$ to enforce Eq. (24) through the orthogonality conditions

$$\int_A \mathrm{d}A_\mathbf{x} \mathbf{N}_l^T(\mathbf{x})\hat{\mathbf{g}}(\mathbf{x}) + \int_A \mathrm{d}A_\mathbf{x} \mathbf{N}_l^T(\mathbf{x})\hat{\mathbf{u}}(\mathbf{x}) = \mathbf{0} \qquad \text{for } l = 1, 2, ..., N \tag{29}$$

where N is the number of nodes on the boundary mesh, and the supra-index T denotes transposition. Taking into account the compact support of the nodal shape functions $\mathbf{N}_l(\mathbf{x})$ and after
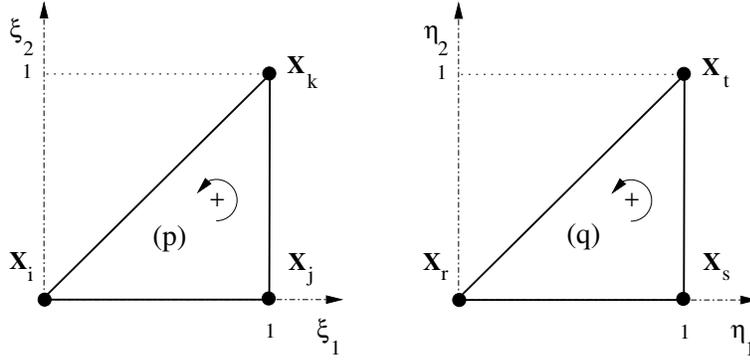
Figure 2: Master triangles p and q for the simplex coordinates.

some algebra (see Appendix), Eq. (29) results in the equation system

$$\sum_{q=1}^{E} \left[\mathbf{I}^{(p,q)} \mathbf{\Psi}^{(q)} + \mathbf{J}^{(p,q)} \mathbf{\Psi}^{(p)} \right] = -\mathbf{M}^{(p)} \mathbf{U}^{(p)} \qquad \text{for } p = 1, 2, ..., E \tag{30}$$

with the short notations

$$\mathbf{I}^{(p,q)} = \int_{A^{(p)}} \mathrm{d}A_{\mathbf{x}} \int_{A^{(q)}} \mathrm{d}A_{\mathbf{y}} \, \mathbf{N}^{(p)T}(\mathbf{x}) \, \mathbf{H}(\mathbf{x}, \mathbf{y}) \, \mathbf{N}^{(q)}(\mathbf{y}) \tag{31}$$

and

$$\mathbf{J}^{(p,q)} = \int_{A^{(p)}} \mathrm{d}A_{\mathbf{x}} \int_{A^{(q)}} \mathrm{d}A_{\mathbf{y}} \, \mathbf{N}^{(p)T}(\mathbf{x}) \, \mathbf{K}(\mathbf{x}, \mathbf{y}) \, \mathbf{N}^{(p)}(\mathbf{x}) \tag{32}$$

for the elements of the matrix system, while the element source vector is given by

$$\mathbf{M}^{(p)} = \int_{A^{(p)}} \mathrm{d}A_{\mathbf{x}} \, \mathbf{N}^{(p)T}(\mathbf{x}) \mathbf{N}^{(p)}(\mathbf{x}) \tag{33}$$

The p and q triangles have the global numbered nodes i, j, k and r, s, t, respectively, see Fig. 2. Then, the element solution vectors in Eq. (30) are given by

$$\mathbf{\Psi}^{(p)} = \begin{bmatrix} \mathbf{\Psi}_i \\ \mathbf{\Psi}_j \\ \mathbf{\Psi}_k \end{bmatrix} \in \mathbb{R}^{9 \times 1} \quad \text{with} \quad \mathbf{\Psi}_i = \begin{bmatrix} \psi_{3i-2} \\ \psi_{3i-1} \\ \psi_{3i} \end{bmatrix} \in \mathbb{R}^{3 \times 1} \tag{34}$$

as well as

$$\mathbf{\Psi}^{(q)} = \begin{bmatrix} \mathbf{\Psi}_r \\ \mathbf{\Psi}_s \\ \mathbf{\Psi}_t \end{bmatrix} \in \mathbb{R}^{9 \times 1} \quad \text{with} \quad \mathbf{\Psi}_r = \begin{bmatrix} \psi_{3r-2} \\ \psi_{3r-1} \\ \psi_{3r} \end{bmatrix} \in \mathbb{R}^{3 \times 1} \tag{35}$$

while the element source vector is

$$\mathbf{U}^{(p)} = \begin{bmatrix} \mathbf{U}_i \\ \mathbf{U}_j \\ \mathbf{U}_k \end{bmatrix} \in \mathbb{R}^{9 \times 1} \quad \text{with} \quad \mathbf{U}_i = \begin{bmatrix} U_{3i-2} \\ U_{3i-1} \\ U_{3i} \end{bmatrix} \in \mathbb{R}^{3 \times 1} \tag{36}$$

3.3 Double-surface integrals over flat triangles with a weak singularity

Each of the interaction integrals $\mathbf{I}^{(p,q)}$ and $\mathbf{J}^{(p,q)}$ given by Eqs. (31) and (32), respectively, involves the double-surface integral

$$\mathbf{Z} = \int_{A^{(p)}} \mathrm{d}A_{\mathbf{x}} \int_{A^{(q)}} \mathrm{d}A_{\mathbf{y}} \, \mathbf{F}(\mathbf{x}, \mathbf{y}) \tag{37}$$

that is performed over the p and q panels, so it is a quadruple integral. The integrand contains the multiplicative kernel $\mathbf{F} = \mathbf{L}\tilde{\mathbf{G}}$, where $\mathbf{L} = \mathbf{L}(\mathbf{x}, \mathbf{y})$ is some multiplicative regular function and $\tilde{\mathbf{G}} = \tilde{\mathbf{G}}(r)$ is the Green function of the problem with $r = \|\mathbf{x} - \mathbf{y}\|_2$ such that it contains a weak singularity $O(1/r)$. Then, Eq. (37) is transformed by using two simplex coordinate sets, i.e. (ξ_1, ξ_2) over the p panel and (η_1, η_2) over the q one,

$$\begin{aligned}
(\xi_1, \xi_2) &: 0 \leq \xi_1 \leq 1 \; ; \; 0 \leq \xi_2 \leq \xi_1 \\
(\eta_1, \eta_2) &: 0 \leq \eta_1 \leq 1 \; ; \; 0 \leq \eta_2 \leq \eta_1
\end{aligned} \tag{38}$$

see Fig. 2. The generic points on each of these triangles are transformed to the p and q panels using

$$\begin{aligned}
\mathbf{x}(\xi_1, \xi_2) &= \mathbf{N}^{(p)}(\xi_1, \xi_2) \mathbf{X}^{(p)} \\
\mathbf{y}(\eta_1, \eta_2) &= \mathbf{N}^{(q)}(\eta_1, \eta_2) \mathbf{X}^{(q)}
\end{aligned} \tag{39}$$

with the element shape functions

$$\begin{aligned}
\mathbf{N}^{(p)}(\xi_1, \xi_2) &= \begin{bmatrix} (1 - \xi_1) & (\xi_1 - \xi_2) & \xi_2 \end{bmatrix} \\
\mathbf{N}^{(q)}(\eta_1, \eta_2) &= \begin{bmatrix} (1 - \eta_1) & (\eta_1 - \eta_2) & \eta_2 \end{bmatrix}
\end{aligned} \tag{40}$$

and the element nodal coordinates at the triangle vertices

$$\mathbf{X}^{(p)} = \begin{bmatrix} \mathbf{X}_i \\ \mathbf{X}_j \\ \mathbf{X}_k \end{bmatrix} \quad ; \quad \mathbf{X}^{(q)} = \begin{bmatrix} \mathbf{X}_r \\ \mathbf{X}_s \\ \mathbf{X}_t \end{bmatrix} \tag{41}$$

Then, Eq. (37) is written as

$$\mathbf{Z} = \int_{A^{(p)}} \mathrm{d}A_{\mathbf{x}} \int_{A^{(q)}} \mathrm{d}A_{\mathbf{y}} \, \mathbf{F}(\mathbf{x}, \mathbf{y}) = J^{(p)} J^{(q)} \, \tilde{\mathbf{F}} \tag{42}$$

where $J^{(p),(q)} = 2A^{(p),(q)}$ are the Jacobians of each panel, and $A^{(p),(q)}$ are their areas, respectively, whereas $\tilde{\mathbf{F}}$ is written in simplex coordinates as

$$\tilde{\mathbf{F}} = \int_0^1 \mathrm{d}\xi_1 \int_0^{\xi_1} \mathrm{d}\xi_2 \int_0^1 \mathrm{d}\eta_1 \int_0^{\eta_1} \mathrm{d}\eta_2 \, \mathbf{F}(\boldsymbol{\xi}, \boldsymbol{\eta}) \tag{43}$$

Further details about a systematic strategy for computing Eq. (43) can be found in Taylor (2003); D'Elía et al. (2009a).

Table 1: Number of nodes N and elements E. Meshes 1-11 are structured on the unit sphere (smooth and perturbed ones) and on the unit cube (smooth only). Mesh 12 is unstructured on the unit cube.

z	1	2	3	4	5	6	7	8	9	10	11	12
N	218	386	602	866	1178	1538	2402	3458	4706	5402	6938	674
E	432	768	1200	1728	2352	3072	4800	6912	9408	10800	13072	1344

3.4 Surface traction field computation

The body force $\mathbf{D} = (D_1, D_2, D_3)$ and torque $\mathbf{C} = (C_1, C_2, C_3)$, with respect to the origin $O(x, y, z)$ of the Cartesian coordinate system, are computed by the surface integrals (Power and Miranda, 1987)

$$
\begin{aligned}
\mathbf{D} &= \int_A \mathrm{d}A_\mathbf{y}\, \boldsymbol{\phi}(\mathbf{y}) \\
\mathbf{C} &= \int_A \mathrm{d}A_\mathbf{y}\, [\mathbf{y} \times \boldsymbol{\phi}(\mathbf{y})]
\end{aligned}
\tag{44}
$$

The traction field $t_i(\mathbf{x}) = \sigma_{ij}(\mathbf{x})n_j(\mathbf{x})$ at the field point $\mathbf{x}$, where $\sigma_{ij}(\mathbf{x})$ is the stress tensor, is obtained using (e.g. Ladyzhenskaya (1969), Sec. 3.2, Eq. 24, p. 58),

$$
t_i(\mathbf{x})_{(e)} = -\frac{1}{2}\phi_i(\mathbf{x}) - \frac{3}{4\pi} \int_A \mathrm{d}A_\mathbf{y} K_{ji}(\mathbf{y}, \mathbf{x})\phi_j(\mathbf{y}) \qquad \text{for } \mathbf{x} \in A
\tag{45}
$$

where $K_{ji}(\mathbf{y}, \mathbf{x})$ is the transposed kernel from Eq. (9), and $\phi_j(\mathbf{y})$ is the single-layer surface density given in Eq. (17). It should be noted that Eq. (45) assumes that the unit normal $\mathbf{n}(\mathbf{x})$ is well defined at the field point $\mathbf{x}$. This restriction precludes the use of this equation for the computation of the traction field at points with geometric discontinuities, such as nodes, edges or vertices of the polyhedral surface mesh, at least in a more classical sense. This shortcoming is avoided by employing the panel centroids as the field points $\mathbf{x}$ in the numerical examples. The drag coefficients are finally obtained as $K = D/(\mu U_\infty L)$, $K_i = D_i/(\mu U_\infty L)$ and $\tilde{K} = C/(\mu U_\infty L^2)$, where U_∞ is the (unperturbed) incoming speed, L is a typical length, $D = \|\mathbf{D}\|_2$, and $C = \|\mathbf{C}\|_2$. The traction coefficients are given by $\tau(\mathbf{x}) = t(\mathbf{x})/(\mu U_\infty L^{-1})$ and $\tau_i(\mathbf{x}) = t_i(\mathbf{x})/(\mu U_\infty L^{-1})$. The subindex $i = 1, 2, 3$ in the drag and traction coefficients indicates the corresponding x_i Cartesian component. In the numerical examples it was verified that the body force obtained by summing the traction field given by Eq. (45) was close to the one obtained with Eq. (44), although only the last ones are shown.

4 NUMERICAL EXAMPLES

Numerical simulations are performed with the proposed scheme for the steady creeping flow of a viscous and incompressible fluid around a single body. Two flow cases are considered, a sphere of unit radius and a cube of unit edge length, whose centers are placed at the origin of the Cartesian coordinate system in $\mathbb{R}^3$. The numerical examples cover issues on the convergence of the numerical solution under mesh refinement, and their numerical stability under small mesh perturbations. In the unit cube example, the traction coefficients are plotted for several flow eigenmodes in order to check the traction laws close to the edges and vertices, by comparison with the semi-analytical computations of Mustakis and Kim (1998). The results of the parallel eigenmode around the unit cube are also compared with a finite element computation. Flat simplex triangles are used in all cases. The number z of BEM meshes and the corresponding number of nodes N and elements E are shown in Table 1, where meshes 1-11 are structured

incoming flow	unperturbed velocity $\mathbf{U}$	force $\mathbf{D}$	torque $\mathbf{C}$
uniform	$(U_\infty, 0, 0)$	$(6\pi\mu U_\infty \mathcal{R}, 0, 0)$	$\mathbf{0}$
shear	$U_\infty(x_2, -x_1, 0)/\mathcal{R}$	$\mathbf{0}$	$(0, 0, 8\pi\mu U_\infty \mathcal{R}^2)$
paraboloid	$U_\infty(x_1^2 + x_2^2, 0, 0)/\mathcal{R}^2$	$(4\pi\mu U_\infty \mathcal{R}, 0, 0)$	$\mathbf{0}$

Table 2: Steady creeping flow around a sphere of radius $\mathcal{R}$. Analytical expressions for the viscous force and torque for different incoming flows (Guazzelli, 2003; Dhont, 1996).
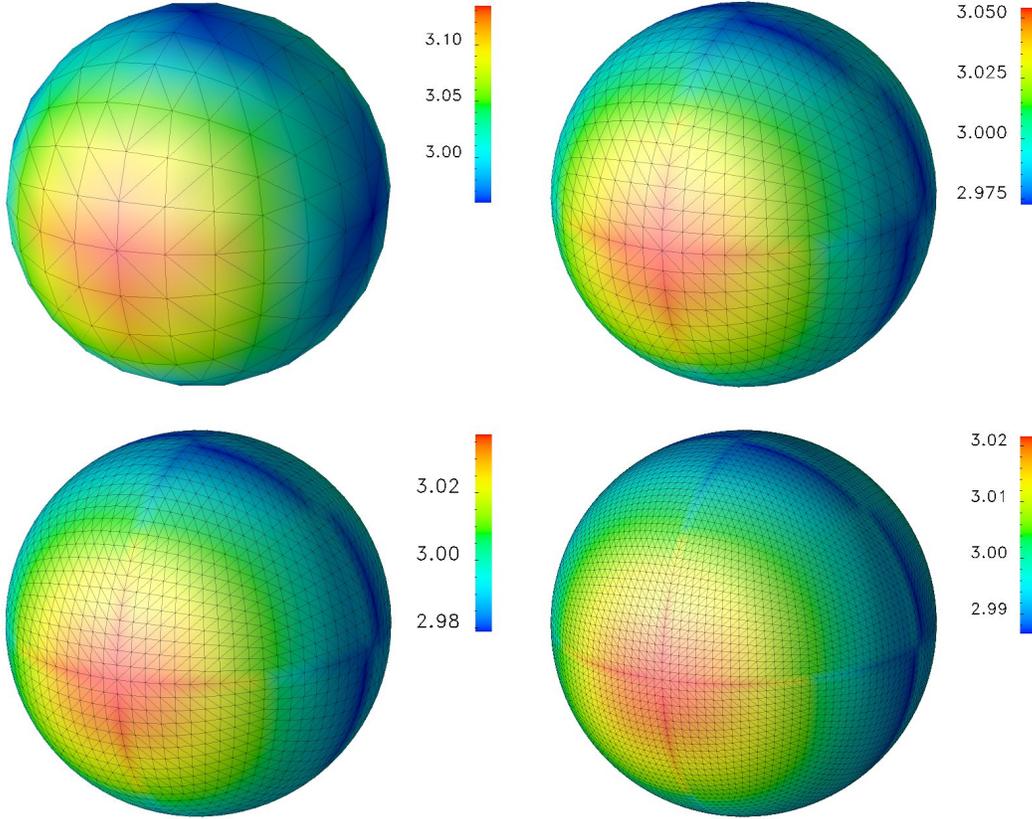
Figure 3: Colormaps of the τ_1 traction coefficient on the unit sphere surface using a Q_{22} quadrature rule and smooth BEM meshes 1, 5, 9 and 11 (see Table 1), from left to right and from top to bottom, respectively.

(smooth and perturbed ones), whereas mesh 12 is an unstructured one only used for the unit cube.

The Gauss-Legendre formula is employed in the modified Taylor "black box" integrator, with n_{1d} quadrature points along each direction which, in turn, implies a total of n_{1d}^4 points by interaction pair. Since the number of quadrature points may change among the panel layers, the notation Q_{IJ} will be introduced, meaning that there are I Gauss-Legendre points on the self-integral and the first layer of neighbouring panels and J points for the remaining layers. The absolute value of the relative error $|e_r|$ for the force coefficient K is computed as $|e_r| = |K_{\text{num}}/K_{\text{(semi)analytical}} - 1|$, and it is plotted as a function of the type of incoming flow, the Q_{IJ} quadrature rule and the number M of the degrees of freedom, being $M = 3E$ and $M = 3N$ in collocation and Galerkin, respectively.
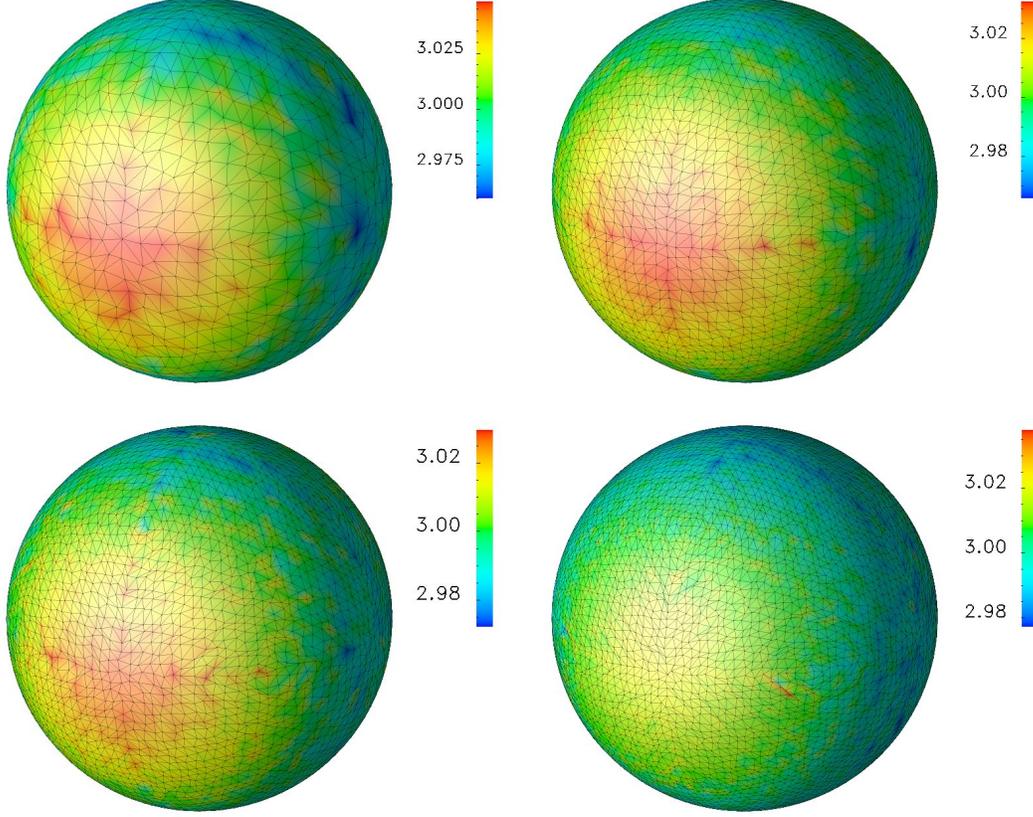
Figure 4: Colormaps of the τ_1 traction coefficient on the unit sphere surface using a Q_{22} quadrature rule and perturbed BEM meshes 6, 8, 9 and 11 (see Table 1), from left to right and from top to bottom, respectively.

4.1 Sphere

The sphere test case is chosen since there are analytical solutions for several inflow conditions. In particular, three inflow conditions are considered: uniform, shear, and paraboloid (Power and Miranda, 1987). Analytical expressions (Guazzelli, 2003; Dhont, 1996) for the unperturbed velocity, the force, and the torque for each case are summarized in Table 2. The following values are adopted in the numerical simulations: fluid density $\rho = 1 \, \text{kg}/\text{m}^3$, kinematic viscosity $\nu = 1 \, \text{m}^2/\text{s}$, incoming speed $U_\infty = 0.01$ m/s along the x direction, and sphere radius $\mathcal{R} = 1$ m, while the sphere diameter is taken as the typical length, i.e. $L = 2\mathcal{R} = 2$ m. The analytical traction field on the sphere surface under uniform flow is the constant value $\mathbf{t} = (3/2)\mu U_\infty/\mathcal{R} \, \mathbf{e}_1^0$, where $\mathbf{e}_1^0$ is the unit Cartesian vector in the x_1 direction and $\mu = \rho\nu = 1 \, \text{kg}/\text{m s}$, which in turn implies the constant traction coefficient $\tau = 3$. Figure 3 shows the colormaps of the τ_1 traction coefficient with the smooth BEM meshes 1, 5, 9 and 11 using a Q_{22} quadrature rule, from left to right and from top to bottom, respectively.

In order to check the numerical stability of the solution, computations have been made over perturbed meshes obtained by small random displacements of the nodal positions without leaving the surface of the unit sphere. Figure 4 shows the colormaps of the traction coefficient for the perturbed BEM meshes 6, 8, 9 and 11.

The absolute value of the relative percent error $|e_r\%|$ of the force coefficient K_i, as a function of the number of degrees of freedom M and the Q_{IJ} quadrature rule, with the smooth meshes on the unit sphere, is plotted in Fig. 5 for three incoming flows: uniform flow (left), shear flow (center) and paraboloid flow (right), respectively, with collocation (top) and Galerkin (bottom)

procedures. Note that the Q_{11} rule gives monotone convergence with a collocation procedure; however, when a Galerkin one is used, this monotone convergence behaviour is obtained for the Q_{22} rule. Furthermore, the order of magnitude of the error with a Q_{22} rule and a Galerkin procedure is smaller than a Q_{11} rule with a collocation one.

The surface friction line patterns of the velocity field close to the unit sphere surface using mesh 8 are plotted in Fig. 6 as follows: uniform flow $(U_\infty, 0, 0)$ m/s (left), shear flow $U_\infty(x_2, -x_1, 0)/\mathcal{R}$ (center), and paraboloid flow $U_\infty(x_1^2 + x_2^2, 0, 0)/\mathcal{R}^2$ (right).

4.2 Steady creeping eigenmodes around the unit cube

As an example of a sharp body, a cube of unit edge length, whose center is placed at the origin in $\mathbb{R}^3$, is considered. The cube test case is selected as a crude simplification of the phenomena appearing with MEMS geometries (Fachinotti et al., 2007; Méndez et al., 2008; Berli and Cardona, 2009). In the numerical simulations, the following values are adopted: fluid density $\rho = 1$ kg/m^3, kinematic viscosity $\nu = 1$ m^2/s, and edge length $L = 1$ m. Following Mustakis and Kim (1998), five flow eigenmodes are next considered.

4.2.1 Parallel and splitting eigenmodes.

The first two flow eigenmodes are sketched in Fig. 7 and they are: (i) the parallel mode $\mathbf{U}_\infty = (1, 0, 0)$ m/s, with flow parallel to edges $J - J'''$, see Fig. 7 (left); and (ii) the splitting mode $\mathbf{U}_\infty = (1, 0, 1)$ m/s, where the flow is splitted by edges $K - K'$ and turns around the edges $L - L'$, see Fig. 7 (right). They are quasi two–dimensional (2D) flow eigenmodes in the sense that a 2D wedge flow approximation can be performed close to the edges $J - J'''$, $K - K'$ and $L - L'$. The edges $K - K'$ have the symmetric flow, while the edges $L - L'$ have the antisymmetric one. Mustakis-Kim computed semianalytical asymptotic laws for the total traction coefficients K, as a function $O(s^p)$ of the distance s to the edge singularities (Mustakis and Kim, 1998). The singularity exponents p found by Mustakis-Kim are: $p = -0.4555$ close to the parallel edges $J - J'''$, $p = -0.0915$ close to the symmetric edges $K - K'$, and $p = -0.3333$ close to the antisymmetric edges $L - L'$, see Fig. 7.

4.2.2 Symmetric and antisymmetric I and II eigenmodes.

The third, fourth and fifth flow eigenmodes are a symmetric and two antisymmetric 3D flows, respectively, not sketched in the figures. In this case, the semianalytical asymptotic laws for the total traction coefficients K are computed as a function $O(s^p)$ of the distance s to a vertex singularity (Mustakis and Kim, 1998). The flow eigenmodes and their singularity exponents p close to, for instance, the vertex M and along the diagonal coordinate WI, see Fig. 8 (right), were also given in Mustakis and Kim (1998) and they are as follows: the symmetric flow with $\mathbf{U}_\infty = (1, 1, 1)$ m/s and $p = -0.31877$, the antisymmetric I flow with $\mathbf{U}_\infty = (1, 0, -1)$ m/s and $p = -0.62463$, and the antisymmetric II flow with $\mathbf{U}_\infty = (1, -2, 1)$ m/s and $p = -0.62463$, respectively, i.e. the antisymmetric flow has a double eigenvalue and two eigenmodes.

4.3 GBEM numerical solution of the steady creeping eigenmodes around the unit cube

Several meshes are used in order to check mesh convergence under refinement along the (polygonal) coordinates: front-meridian AB, rear-meridian CD, equatorial EF and diagonal WI, see Fig. 8. Comparisons between Mustakis-Kim asymptotic laws and a GBEM computation with a Q_{22} quadrature rule on mesh 11 are shown in Figs. 9 and 10. It should be noted that

Mustakis-Kim give only the traction law as a function of the distance s to the edge or vertex singularity and, then, only this dependence is plotted in all figures.

In the case of the quasi two–dimensional steady creeping eigenmodes, the total traction coefficients K across the middle cube section parallel to the unperturbed flow are plotted in Fig. 9 as a function of the (polygonal) coordinates: (i) front-meridian AB (left), rear-meridian CD (center), and equatorial EF (right). The total traction coefficients K for the three–dimensional steady creeping eigenmodes of the 90 degree vertex are plotted in Fig. 10 as a function of the (polygonal) coordinate along the diagonal WI coordinate on the top plane. In the case of flow parallel to edges J-J''' (parallel mode $U_\infty = (1, 0, 0)$ m/s, Fig. 9), the total traction coefficient computed in the x_1-Cartesian direction is, approximately, $K_1 \approx 12.70$ using the mesh 11.

The colormaps of the τ_1 traction coefficient on the unit cube surface obtained with meshes 12 and 10 are shown in Fig. 11, left and right, respectively.

4.4 Analysis of the convergence under mesh refinement

The absolute value of the relative errors $|e_r|$ of the force coefficient K_i on the unit sphere, using the Q_{22} quadrature rule are plotted, respectively for smooth and noisy meshes, in Figs. 12 and 13, and for incoming flow types: $e_r(K_1)$ uniform flow (left), $e_r(K_3)$ shear flow (middle) and $e_r(K_1)$ paraboloid flow (right). Galerkin BEM results are displayed with a solid line, while results obtained with collocation BEM are plotted with a dashed line. Note that with GBEM the convergence is monotone and almost linear whereas collocation BEM does not show a monotonic convergence.

Since there is no analytical solution for the unit cube, bounds and semi–numerical values are taken as a reference. For instance, the drag force is bounded (Mestel, 2004) by $D_{\min} < D < D_{\max}$, with $D_{\min} = 3\pi\mu U_\infty L$ and $D_{\max} = \sqrt{3}D_{\min}$, where L is the cube edge length, and $U_\infty = ||\mathbf{U}_\infty||_2$. The corresponding drag coefficient interval is $K_{\min} < K < K_{\max}$, with $K_{\min} = 3\pi$ and $K_{\max} = 3\sqrt{3}\pi$. The relative errors computed taking as reference the results from the more refined mesh (mesh 11) are plotted in Fig. 14 with a Galerkin BEM (solid line) and with a collocation BEM (dashed line) for: uniform flow (left), shear flow (middle) and paraboloid flow (right).

The drag coefficients obtained with the more refined mesh (mesh 11, Table 1) are: $K_1 \approx 12.70$, $K_3 \approx 8.03$ and $K_1 \approx 3.63$ for uniform, shear and paraboloid incoming flows, respectively. It is worth noting that the drag coefficients obtained in the uniform flow case are close to the geometric mean $K_{\mathrm{gm}} = (K_{\min} K_{\max})^{1/2}$ given by $K_{\mathrm{gm}} = 3\pi\sqrt[4]{3} \approx 12.404$.

4.5 Performance issues between collocation and Galerkin BEM techniques

Comparing performance issues between the present collocation and Galerkin implementations, it can be observed that: (i) the net forces obtained with a Galerkin BEM are a bit more accurate than that obtained with collocation BEM; (ii) the Galerkin BEM exhibits monotonic convergence while a collocation BEM does not have this property; (iii) the system matrix with a Galerkin BEM is symmetric whereas with collocation BEM does not have this property; (iv) the size of the solution vector $\mathbf{\Psi}$ is $3N$ with a Galerkin BEM and $3E$ with a collocation BEM and, since $N \ll E$ for 2D BEM meshes immersed in 3D, then the Galerkin BEM is relatively cheaper than collocation BEM in core-memory resources, especially when dense matrices are employed. For instance, in the case of mesh 11 in Table 1, there are 20 814 unknowns when using Galerkin ($3N$) and 39 216 ones when using collocation ($3E$), i.e. approximately a ratio of 2 to 1, and, therefore, a Galerkin approach allows to use more refined meshes for a given size

of the core memory.

The surface friction line patterns of the velocity field close to the unit cube surface using mesh 8 are plotted in Fig. 15 as follows. At the top: parallel mode $\mathbf{U}_\infty = (1, 0, 0)$ m/s (left), splitting mode $\mathbf{U}_\infty = (1, 0, 1)$ m/s (center) and symmetric mode $\mathbf{U}_\infty = (1, 1, 1)$ m/s (right). At the bottom: antisymmetric I mode $\mathbf{U}_\infty = (1, 0, -1)$ m/s (left), antisymmetric II mode $\mathbf{U}_\infty = (1, -2, 1)$ m/s (center), and shear flow $\mathbf{U}_\infty = (x_2, -x_1, 0)/L$ m/s (right).

4.6 FEM numerical solution of the parallel creeping eigenmode around the unit cube

In order to provide another validation, a FEM computation of the parallel mode $\mathbf{U}_\infty = (U_\infty, 0, 0)$ is performed using the open source PETSc-FEM code, which is a parallel multi-physics finite element library (Storti et al., 2008; Storti and D'Elía, 2004; Battaglia et al., 2006, 2010; Garibaldi et al., 2008; Dalcín et al., 2007; Franck et al., 2009) based on the Message Passing Interface (MPI, http://www.mpi-forum.org) and the Portable Extensible Toolkit for Scientific Computations (PETSc, http://www-fp.mcs.anl.gov/petsc). This code solves the Navier-Stokes equations using the SUPG/PSPG algorithm (Tezduyar et al., 1992; Sonzogni et al., 2002), i.e. using equal-order interpolations with the PSPG stabilization term in order to satisfy the Brezzi-Babuška condition. The FEM computation includes the inertial terms, so that in order to compare it with the GBEM results a low Reynolds number is chosen.

The only flow case considered in the FEM computation is the parallel mode $\mathbf{U}_\infty = (U_\infty, 0, 0)$ m/s, with flow parallel to the edges J-J''', see Fig. 7 (left). The Reynolds number is set to 0.001 by choosing the particular combination of parameters: kinematic fluid viscosity $\nu = 0.1$ m^2/s, incoming speed $U_\infty = 10^{-4}$ m/s and cube side lenght $L = 1$ m. The flow is aligned with the x axis and, by symmetry considerations, only one fourth of the domain ($y, z \geq 0$) is considered. The finite element mesh is constructed by extrusion of a surface mesh having 50x50 quadrangles on each side of the cube, i.e. it has $50 \times 50 \times 6/4 = 3750$ quadrangles on 1/4 of the cube inside a prismatic domain. The nodal spacing is non-uniform, with a logarithmic refinement towards the edges of the cube, where the results show large friction values. This refinement is such that the linear size h of the quadrangles near the center of the face is in a ratio of 5:1 to the size near the edges. The surface mesh is extruded into 50 layers of hexahedral elements in the radial direction from the cube surface, up to an external cube of length $L_{\text{ext}} = 50$ m. The width of layers in the radial direction is also refined towards the internal cube surface in such a way that the width of the external layer is in a ratio of 40:1 to the layer adjacent to the cube skin. Boundary conditions are as follows: velocity $\mathbf{U} = \mathbf{U}_\infty$ m/s at inlet ($x = -L_{\text{ext}}/2$), pressure $p = 0$ at outlet ($x = L_{\text{ext}}/2$), slip boundary condition at the lateral walls $y, z = \pm L_{\text{ext}}/2$, and non-slip boundary condition $\mathbf{U} = \mathbf{0}$ at the cube.

With this setup the computed value for the drag is $K_1 = F_1/(\mu U_\infty L) \approx 13.76$. The numerical experiment is performed with other values of L_{ext} and mesh refinement in order to assess the sensitivity of this result with respect to those parameters. These series of experiments have shown that this result is particularly sensitive to the size of the computational domain L_{ext}. This is so because the slip boundary conditions are equivalent to a lattice of mirrors of the cube with a spacing of $\Delta y = \Delta z = L_{\text{ext}}$ Then, each cube sees an effective external field given by U_∞ plus the velocity induced by the other cubes in the array. This field decays very slowly (as $O(1/L_{\text{ext}})$) for $L_{\text{ext}} \to \infty$, so that very large domains must be used in order to reduce the error. For instance, the error for $L_{\text{ext}} = 10$ is estimated in 15%. Computations for a sphere, for which the drag can be computed analytically, show a similar behavior.

The traction map obtained with GBEM is close to the FEM one, whereas the traction coefficient is approximately 8% lower than the FEM value. This difference deserves some comments.

Both results fall within the interval $(K_{\min}, K_{\max})$ predicted by an analytic computation. In the computation with GBEM, the result is sensitive to the number of quadrature points, whereas for FEM the most influential parameter is the size of the computational domain. In both cases, some residual error may be due to insufficient mesh refinement. This is especially true in the FEM case, because the strong variation of friction near the edges degrades the convergence with respect to the mesh refinement. Figure 16 shows the Cartesian K_1 component of the traction coefficient of the parallel mode $\mathbf{U}_\infty = (U_\infty, 0, 0)$, as a function of the meridian (polygonal) coordinate s_m (left), and as a function of the equatorial one s_e (right), obtained with FEM (solid line) and GBEM (crosses) computation.

5 CONCLUSIONS

An indirect boundary integral equation of Fredholm type and second kind has been developed for exterior and steady Stokes flow around a three-dimensional rigid body, and it has been numerically solved using collocation and Galerkin procedures. The boundary integral equation has been chosen as a combination of double- and single- layer potentials for steady creeping flows with densities defined over the closed surface. It is an extension of the "completed double-layer boundary integral equation method" (e.g. Power and Wrobel (1995); Kim and Karrila (1991)). Unlike the original version, in the present strategy a surface single-layer density, equivalent to a surface density of Stokeslets, has been used and, since a distributed system of point forces can exert a net torque, it has not been necessary to introduce a surface density of rotlets. The rigid body motions have been excluded assuming that the single-layer density has a linear dependence with respect to the double-layer one through the ad hoc Eq. (16), following an idea introduced in Power and Miranda (1987) and extensively reviewed in Kim and Karrila (1991). The double surface integrals that express the pairwise interaction among all boundary elements have been approximated using a modified Taylor integration scheme (Taylor, 2003; D'Elía et al., 2009a), and a Q_{IJ} strategy, with I Gauss-Legendre points on the self-integral and first layer of neighbouring panels, those that have a common edge or vertex, and J ones for the remaining layers, on each integration coordinate. The numerical examples included the steady creeping flow around the unit radius sphere and the unit edge length cube, covering issues on the convergence under mesh refinement and numerical stability under small mesh perturbations. Gauss–Legendre quadrature points $n_{1d} = \{1, 2\}$ along each direction have been used which, in turn, imply a total of n_{1d}^4 points by pair interaction. From the numerical tests with the sphere, it was noted that the Q_{11} rule gives monotone convergence with a collocation BEM. However, when a Galerkin BEM was used, this monotone convergence behaviour was obtained for the Q_{22} rule. Furthermore, the order of magnitude of the error with a Q_{22} rule and a Galerkin procedure is smaller than a Q_{11} rule with a collocation one. When the boundary mesh was refined enough, a Q_{12} quadrature rule has been found to give a reasonable approximation and, then, it can be a compromise solution for highly refined meshes. In any case, the system matrix obtained with a Galerkin technique remains fully populated, as in most standard BEM schemes; however, it is symmetric and positive defined which enables a better coupling of BEM and FEM matrices. The singular behavior of the surface traction on edges and corners in the unit cube test for steady creeping eigenmodes has been close to the singularity exponents obtained with a semi- analytical computation of Mustakis and Kim (1998). The parallel eigenmode, with parallel flow along the cube edges, has been also compared with a finite element computation. The colormaps of the surface traction and the friction line pattern of the velocity field near edges and corners have not shown numerical instabilities nor severe precision loss; although, the traction field has been somewhat smoothed.

A APPENDIX. GALERKIN APPROXIMATION THROUGH PIECEWISE SHAPE FUNCTIONS

Linear approximations $\hat{\boldsymbol{\psi}}^{(p)}$ and $\hat{\mathbf{u}}^{(p)}$ for the density $\boldsymbol{\psi}(\mathbf{x})^{(p)} \in \mathbb{R}^{3 \times 1}$ and velocity $\mathbf{u}(\mathbf{x})^{(p)} \in \mathbb{R}^{3 \times 1}$ fields are assumed, respectively, on the surface of the p and q simplex triangles, with nodes i, j, k and r, s, t, respectively, see Fig. 2, that is,

$$\boldsymbol{\psi}^{(p)}(\mathbf{x}) \approx \hat{\boldsymbol{\psi}}^{(p)} = \mathbf{N}^{(p)}(\mathbf{x})\boldsymbol{\Psi}^{(p)}$$
$$\boldsymbol{\psi}^{(q)}(\mathbf{x}) \approx \hat{\boldsymbol{\psi}}^{(q)} = \mathbf{N}^{(q)}(\mathbf{x})\boldsymbol{\Psi}^{(q)} \tag{A1}$$

where the element shape functions $\mathbf{N}^{(p,q)}(\mathbf{x}) \in \mathbb{R}^{3 \times 9}$ are given by

$$\mathbf{N}^{(p)}(\mathbf{x}) = \begin{bmatrix} \mathbf{N}_i^{(p)}(\mathbf{x}) & \mathbf{N}_j^{(p)}(\mathbf{x}) & \mathbf{N}_k^{(p)}(\mathbf{x}) \end{bmatrix}$$
$$\mathbf{N}^{(q)}(\mathbf{x}) = \begin{bmatrix} \mathbf{N}_r^{(q)}(\mathbf{x}) & \mathbf{N}_s^{(q)}(\mathbf{x}) & \mathbf{N}_t^{(q)}(\mathbf{x}) \end{bmatrix} \tag{A2}$$

respectively, which are the restrictions of the nodal shape functions $\mathbf{N}_i(\mathbf{x})$, $\mathbf{N}_j(\mathbf{x})$ and $\mathbf{N}_k(\mathbf{x})$ on the p element, and $\mathbf{N}_r(\mathbf{x})$, $\mathbf{N}_s(\mathbf{x})$ and $\mathbf{N}_t(\mathbf{x})$ on the q element, respectively (Fig. 2), while $\boldsymbol{\Psi}^{(p)}$ and $\boldsymbol{\Psi}^{(q)}$ are given by Eqs. (34) and (35), respectively. The nodal shape functions on Eq. (29) are arranged as

$$\mathbf{N}^T(\mathbf{x}) = \begin{bmatrix} \mathbf{N}_1^T(\mathbf{x}) \\ \dots \\ \mathbf{N}_l^T(\mathbf{x}) \\ \dots \\ \mathbf{N}_N^T(\mathbf{x}) \end{bmatrix} \in \mathbb{R}^{3N \times 3} \quad \text{with} \quad \mathbf{N}_l^T(\mathbf{x}) = \begin{bmatrix} N_l(\mathbf{x}) & 0 & 0 \\ 0 & N_l(\mathbf{x}) & 0 \\ 0 & 0 & N_l(\mathbf{x}) \end{bmatrix} \tag{A3}$$

for nodes $1 \le l \le N$, with

$$N_l(\mathbf{x}) = \sum_{e \in \text{patch(l)}} N_l^{(e)}(\mathbf{x}) \tag{A4}$$

where patch(l) is the patch of adjacent elements around the l node. Then, the functions $\hat{\mathbf{g}}(\mathbf{x}), \hat{\mathbf{u}}(\mathbf{x}) \in \mathbb{R}^{3 \times 1}$ in Eq. (29) are given by

$$\mathbf{g}(\mathbf{x}) \approx \hat{\mathbf{g}}(\mathbf{x}) = \sum_{q=1}^{E} \hat{\mathbf{g}}^{(q)}(\mathbf{x}) \tag{A5}$$

and

$$\mathbf{u}(\mathbf{x}) \approx \hat{\mathbf{u}}(\mathbf{x}) = \sum_{q=1}^{E} \hat{\mathbf{u}}^{(q)}(\mathbf{x}) = \sum_{q=1}^{E} \mathbf{N}^{(q)}(\mathbf{x})\mathbf{U}^{(q)} \tag{A6}$$

respectively, where

$$\hat{\mathbf{g}}^{(q)}(\mathbf{x}) = \int_{A^{(q)}} dA_{\mathbf{y}} \left[\mathbf{H}(\mathbf{x}, \mathbf{y})\hat{\boldsymbol{\psi}}^{(q)}(\mathbf{y}) + \mathbf{K}(\mathbf{x}, \mathbf{y})\hat{\boldsymbol{\psi}}^{(q)}(\mathbf{x}) \right] \tag{A7}$$

and $\mathbf{U}^{(q)}$ is given by

$$\mathbf{U}^{(q)} = \begin{bmatrix} \mathbf{U}_r \\ \mathbf{U}_s \\ \mathbf{U}_t \end{bmatrix} \in \mathbb{R}^{9 \times 1} \quad \text{with} \quad \mathbf{U}_r = \begin{bmatrix} U_{3r-2} \\ U_{3r-1} \\ U_{3r} \end{bmatrix} \in \mathbb{R}^{3 \times 1} \tag{A8}$$

Replacing Eqs. (A5) and (A6) into Eq. (29) results

$$\hat{\mathbf{G}}^{(p)} + \hat{\mathbf{B}}^{(p)} = \mathbf{0} \qquad \text{for } p = 1, 2, ...E \tag{A9}$$

The first term of Eq. (A6) gives the left hand side of the Galerkin system and it is given by

$$
\begin{aligned}
\hat{\mathbf{G}}^{(p)} &= \int_{A^{(p)}} \mathrm{d}A_{\mathbf{x}} \, \mathbf{N}^{(p)T}(\mathbf{x}) \sum_{q=1}^{E} \hat{\mathbf{g}}^{(q)}(\mathbf{x}) \\
&= \int_{A^{(p)}} \mathrm{d}A_{\mathbf{x}} \, \mathbf{N}^{(p)T}(\mathbf{x}) \sum_{q=1}^{E} \int_{A^{(q)}} \mathrm{d}A_{\mathbf{y}} \left[\mathbf{H}(\mathbf{x}, \mathbf{y}) \hat{\boldsymbol{\psi}}^{(q)}(\mathbf{y}) + \mathbf{K}(\mathbf{x}, \mathbf{y}) \hat{\boldsymbol{\psi}}^{(q)}(\mathbf{x}) \right] \\
&= \hat{\mathbf{G}}_1^{(p)} + \hat{\mathbf{G}}_2^{(p)}
\end{aligned}
\tag{A10}
$$

where

$$
\begin{aligned}
\hat{\mathbf{G}}_1^{(p)} &= \sum_{q=1}^{E} \int_{A^{(p)}} \mathrm{d}A_{\mathbf{x}} \int_{A^{(q)}} \mathrm{d}A_{\mathbf{y}} \, \mathbf{N}^{(p)T}(\mathbf{x}) \, \mathbf{H}(\mathbf{x}, \mathbf{y}) \, \mathbf{N}^{(q)}(\mathbf{y}) \, \boldsymbol{\Psi}^{(q)} \\
&= \sum_{q=1}^{E} \mathbf{I}^{(p,q)} \, \boldsymbol{\Psi}^{(q)}
\end{aligned}
\tag{A11}
$$

and

$$
\begin{aligned}
\hat{\mathbf{G}}_2^{(p)} &= \sum_{q=1}^{E} \int_{A^{(p)}} \mathrm{d}A_{\mathbf{x}} \int_{A^{(q)}} \mathrm{d}A_{\mathbf{y}} \, \mathbf{N}^{(p)T}(\mathbf{x}) \, \mathbf{K}(\mathbf{x}, \mathbf{y}) \, \mathbf{N}^{(p)}(\mathbf{x}) \, \boldsymbol{\Psi}^{(p)} \\
&= \sum_{q=1}^{E} \mathbf{J}^{(p,q)} \, \boldsymbol{\Psi}^{(p)}
\end{aligned}
\tag{A12}
$$

where $\mathbf{I}^{(p,q)}$ and $\mathbf{J}^{(p,q)}$ are given by Eqs. (31) and (32), respectively. Finally, the second term of Eq. (A6) gives the right hand side of the Galerkin system and it is given by

$$
\begin{aligned}
\hat{\mathbf{B}}^{(p)} &= \int_{A^{(p)}} \mathrm{d}A_{\mathbf{x}} \, \mathbf{N}^{(p)T}(\mathbf{x}) \sum_{q=1}^{E} \hat{\mathbf{u}}^{(q)}(\mathbf{x}) \\
&= \int_{A^{(p)}} \mathrm{d}A_{\mathbf{x}} \, \mathbf{N}^{(p)T}(\mathbf{x}) \sum_{q=1}^{E} \mathbf{N}^{(q)}(\mathbf{x}) \, \mathbf{U}^{(q)} \\
&= \sum_{q=1}^{E} \int_{A^{(p)}} \mathrm{d}A_{\mathbf{x}} \, \mathbf{N}^{(p)T}(\mathbf{x}) \, \mathbf{N}^{(q)}(\mathbf{x}) \, \mathbf{U}^{(q)} \\
&= \int_{A^{(p)}} \mathrm{d}A_{\mathbf{x}} \, \mathbf{N}^{(p)T}(\mathbf{x}) \, \mathbf{N}^{(p)}(\mathbf{x}) \, \mathbf{U}^{(p)} \\
&= \mathbf{M}^{(p)} \, \mathbf{U}^{(p)}
\end{aligned}
\tag{A13}
$$

where $\mathbf{M}^{(p)}$ is given by Eq. (33).

REFERENCES

Alia A., M. S., and Erchiqui F. Variational boundary element acoustic modelling over mixed quadrilateral–triangular element meshes. *Comm. Numer. Meth. Engng.*, 22(7):767–780, 2006.

Battaglia L., D'Elía J., Storti M.A., and Nigro N.M. Numerical simulation of transient free surface flows. *ASME-Journal of Applied Mechanics*, 73(6):1017–1025, 2006.

Battaglia L., Storti M., and D'Elía J. Bounded renormalization for level set methods. *International Journal for Numerical Methods in Engineering*, 2010. Aceptado.

Beer G. and Watson J. *Introduction to Finite and Boundary Element Method for Engineers*. John Wiley and Sons, England, 1992.

Berli C. and Cardona A. On the calculation of viscous damping of microbeam resonators in air. *Journal of Sound and Vibration*, 327(1-2):249–253, 2009.

Bonnet M., Maier G., and Polizzotto C. Symmetric Galerkin boundary element methods. *Appl. Mech. Rev.*, 51(11):669–704, 1998.

Burghignoli P., Pajewski L., Frezza F., and Galli A. Improved quadrature formulas for boundary integral equations with conducting or dielectric edge singularities. *IEEE Trans. on Antennas and Propag.*, 52(2):373–379, 2004.

Dalcín L., Paz R.R., Storti M., and D'Elía J. MPI for Python: Performance Improvements and MPI-2 Extensions. *Journal of Parallel and Distributed Computing*, 68(5):655–662, 2007.

D'Elía J., Battaglia L., Cardona A., and Storti M. Full numerical quadrature of weakly singular double surface integrals in Galerkin boundary element methods. *Comm. Numer. Meth. Engng.*, 2009a. Doi:10.1002/cnm.1309, in press.

D'Elía J., Battaglia L., Storti M., and Cardona A. Galerkin boundary integral equations applied to three dimensional Stokes flows. In Bauza, Lotito, Parente, and Vénere, editors, *Mecánica Computacional, vol. XXVIII*, pages 1453–1462. Tandil, 2009b.

D'Elía J., Storti M., and Idelsohn S. A closed form for low order panel methods. *Advances in Engineering Software*, 31(5):335–341, 2000a.

D'Elía J., Storti M.A., and Idelsohn S.R. Iterative solution of panel discretizations for potential flows. The modal/multipolar preconditioning. *Int. J. Num. Meth. Fluids*, 32(1):1–22, 2000b.

Dhont J.K.G. *An Introduction to Dynamics of Colloids*. Elsevier, 1996.

Dimitrov A. On singularities in the solution of three-dimensional Stokes flow and incompressible elasticity problems with corners. *International Journal for Numerical Methods in Engineering*, 60(4):773–801, 2004.

Dimitrov A., Andrä H., and Schnack E. Efficient computation of order and mode of corner singularities in 3d-elasticity. *Int. J. for Num. Meth. in Engng.*, 52(8):805–827, 2001.

Duffy M.G. Quadrature over a pyramid or cube of integrands with a singularity at a vertex. *SIAM Journal on Numerical Analysis*, 19(6):1260–1262, 1982.

Eibert T.F. and Hansen V. On the calculation of potential integrals for linear source distributions on triangular domains. *IEEE Trans. on Antennas and Propag.*, 43(12):1499–1502, 1995.

Fachinotti V., Cardona A., D'Elía J., and Paquay S. BEM for the analysis of fluid flow around MEMS. In S.A. Elaskar, E.A. Pilotta, and G.A. Torres, editors, *Mecánica Computacional, vol. XXIV*, pages 1104–1119. Córdoba, Argentina, 2007.

Fata S.N. Explicit expressions for 3D boundary integrals in potential theory. *Int. J. for Num. Meth. in Engng.*, 78:32–47, 2009.

Franck G., Nigro N., Storti M., and D'Elía J. Numerical simulation of the Ahmed vehicle model near–wake. *Latin American Applied Research*, 39(4), 2009. 295-306.

Frangi A. and Bonnet M. A Galerkin symmetric and direct BIE method for Kirchhoff elastic

plates: formulation and implementation. *Int. J. for Num. Meth. in Engng.*, 41(2):337–369, 1998.

Garibaldi J., Storti M., Battaglia L., and D'Elía J. Numerical simulations of the flow around a spinning projectil in subsonic regime. *Latin American Applied Research*, 38(3):241–247, 2008.

Guazzelli E. Microhydrodynamique. cours de base sur les suspensions, 2003. Course notes, Groupe Ecoulements de Particules (GEP), IUSTI, Polytech Marseille.

Hackbusch W. *Integral equations*. Birkhäuser, 1995.

Kim S. and Karrila S.J. *Microhydrodynamics: Principles and Selected Applications*. Butterwoth-Heinemann, 1991.

Kozlov V., Maz'ya V.G., and Rossmann J. *Spectral problems associated with corner singularities of solutions to elliptic equations*. AMS Bookstore, 2001.

Ladyzhenskaya O.A. *The Mathematical Theory of Viscous Incompressible Flow*. Gordon and Breach Science Publishers, 2 edition, 1969.

López-Peña S. and Mosig J.R. Analytical evaluation of the quadruple static integrals on rectangular domains to tolve 3-d electromagnetic problems. *IEEE Trans. on Magnetics*, 45(3):1320–1323, 2009.

Mazza M., Leonetti L., and Aristodemo M. Analytical integration of singular kernels in symmetric boundary element analysis of Kirchhoff plates. *Int. J. for Num. Meth. in Engng.*, 76(2):127–155, 2008.

Medina D. and Liggett J. Three-dimensional boundary element computation of potential flow in fractured rock. *Int. J. for Num. Meth. in Eng.*, 26:2319–2330, 1988.

Méndez C., Paquay S., Klapka I., and Raskin J.P. Effect of geometrical nonlinearity on MEMS thermoelastic damping. *Nonlinear Analysis: Real World Applications*, 10(3):1579–1588, 2008.

Mestel A.J. Viscous Flow, question 3, examination. Technical report, Imperial College London, London, 2004.

Mustakis I. and Kim S. Microhydrodynamics of sharp corners and edges: traction singularities. *AIChE Journal*, 44(7):1469–1483, 1998.

Paquay S. *Développement d'une méthodologie de simulation numérique pour les problèmes vibro-acoustiques couplés intérieurs/extérieurs de grande taille*. Ph.D. thesis, Faculté des Sciences Appliquées, Liège, Belgium, 2002.

Power H. and Miranda G. Second kind integral equation formulation of Stokes flows past a particle of arbitrary shape. *SIAM J. Appl. Math.*, 47(4):689–698, 1987.

Power H. and Wrobel L. *Boundary Integral Methods in Fluid Mechanics*. Computational Mechanics Publications, Southampton,UK, 1995.

Pozrikidis C. *Introduction to Theoretical and Computational Fluid Dynamics*. Oxford, 1996.

Schindler M. *Free surface microflows and particle transport*. Ph.D. thesis, Augsburg Univ., Augsburg, Germany, 2006.

Schuhmacher A. *Sound source reconstruction using inverse sound field calculations*. Ph.D. thesis, Department of Acoustic Technology, Technical University of Denmark, Lyngby, Denmark, 2000.

Scuderi L. On the computation of nearly singular integrals in 3D BEM collocation. *Int. J. for Num. Meth. in Engng.*, 74:1733–1770, 2008.

Sievers D., Eibert T.F., and Hansen V. Correction to "On the calculation of potential integrals for linear source distributions on triangular domains". *IEEE Trans. on Antennas and Propag.*, 53(9):3113–3113, 2005.

Sonzogni V., Yommi A., Nigro N., and Storti M. A parallel finite element program on a Beowulf Cluster. *Advances in Engineering Software*, 33:427–443, 2002.

Stenroos M. and Haueisen J. Boundary element computations in the forward and inverse problems of electrocardiography: comparison of collocation and Galerkin weightings. *IEEE Trans. on Biomedical Engng.*, 55(9):2124–2133, 2008.

Storti M.A. and D'Elía J. Added mass of an oscillating hemisphere at very-low and very-high frequencies. *ASME, Journal of Fluids Engineering*, 126(6):1048–1053, 2004.

Storti M.A., Nigro N.M., Paz R., and Dalcín L.D. Dynamic boundary conditions in computational fluid dynamics. *Comp. Meth. in Appl. Mech. and Engr.*, 197(13–16):1219–1232, 2008. doi:10.1016/j.cma.2007.10.014.

Sutradhar A., Paulino G.H., and Gray L.J. *Symmetric Galerkin Boundary Element Method*. Springer, 2008.

Taylor D.J. Accurate and efficient numerical integration of weakly singulars integrals in Galerkin EFIE solutions. *IEEE Trans. on Antennas and Propag.*, 51(7):1630–1637, 2003.

Tezduyar T.E., Mittal S., Ray S., and Shih R. Incompressible flow computations with stabilized bilinear and linear equal order interpolation velocity-pressure elements. *Comp. Meth. App. Mech. Engng.*, 95:221–242, 1992.

Vodiǎcka R., Mantič V., and París F. On the removal of the non-uniqueness in the solution of elastostatic problems by symmetric Galerkin BEM. *Int. J. for Num. Meth. in Engng.*, 66(12):1884–1912, 2006.

Wang X. *Fast Stokes: A Fast 3-D Fluid Simulation Program for Micro-Electro-Mechanical Systems*. Ph.D. thesis, MIT, 2002.
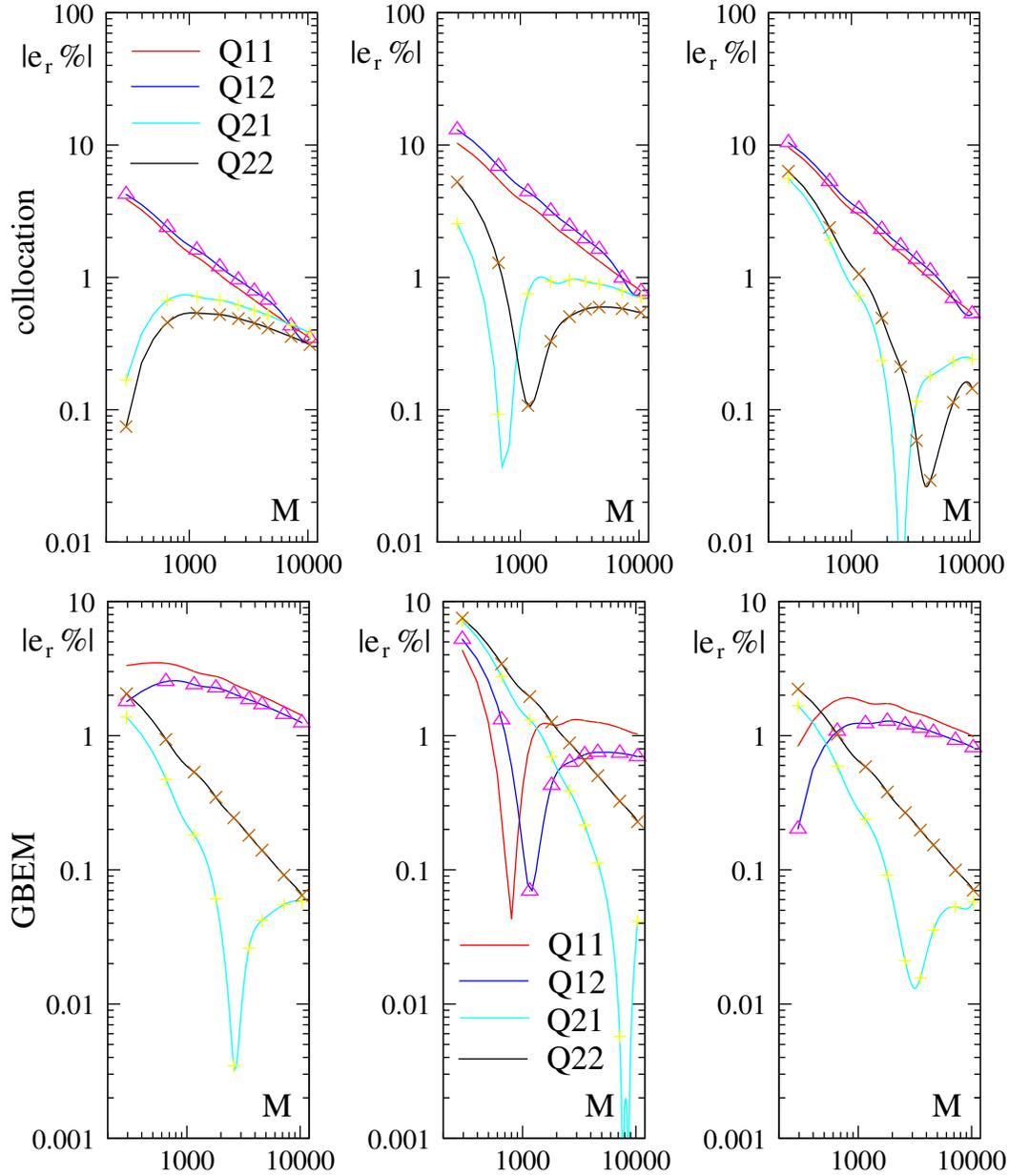
Figure 5: Absolute value of the relative percent error $|e_r\%|$ of the force coefficient K_i as function of the number of degrees of freedom M and the Q_{IJ} quadrature rule with smooth meshes on the unit sphere: K_1 uniform flow (left), K_3 shear flow (center) and K_1 paraboloid flow (right). Collocation (top) and GBEM (bottom).
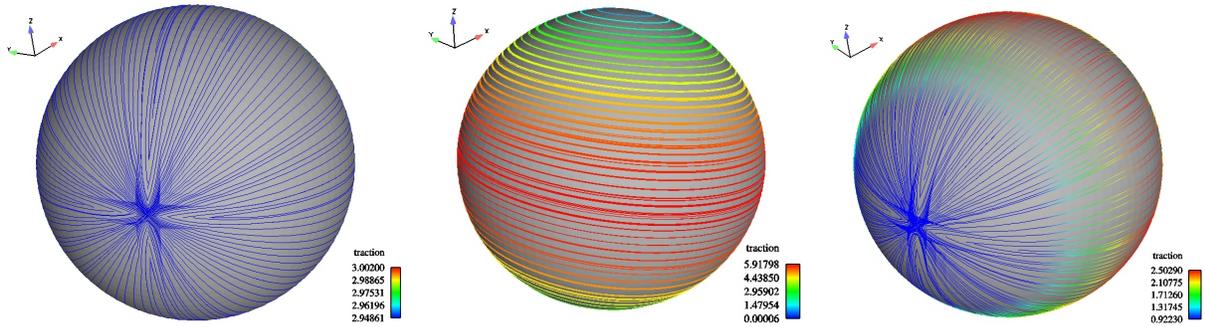
Figure 6: Surface friction line patterns of the velocity field close to the unit sphere surface using a Q_{22} quadrature rule and mesh 8: uniform flow (left), shear flow (center) and paraboloid flow (right).
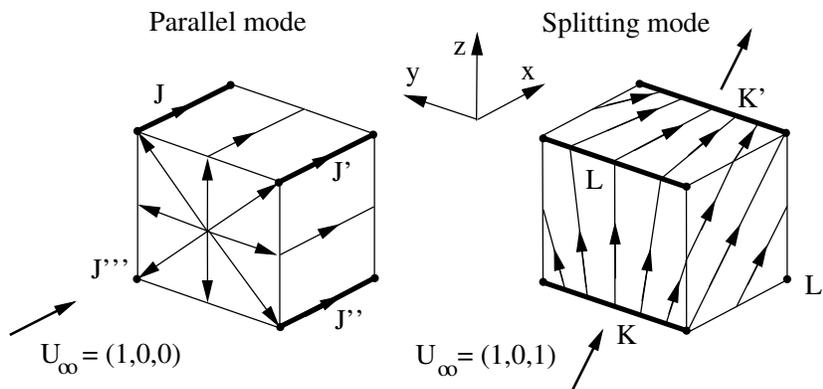
Figure 7: Sketch of the quasi 2D steady creeping eigenmodes across the unit cube: (i) parallel mode $\mathbf{U}_\infty = (1, 0, 0)$ m/s with parallel flow along edges $J - J'''$; (ii) splitting mode $\mathbf{U}_\infty = (1, 0, 1)$ m/s, with symmetric flow along edges K, K' and antisymmetric on edges L, L', as defined in Mustakis and Kim (1998).
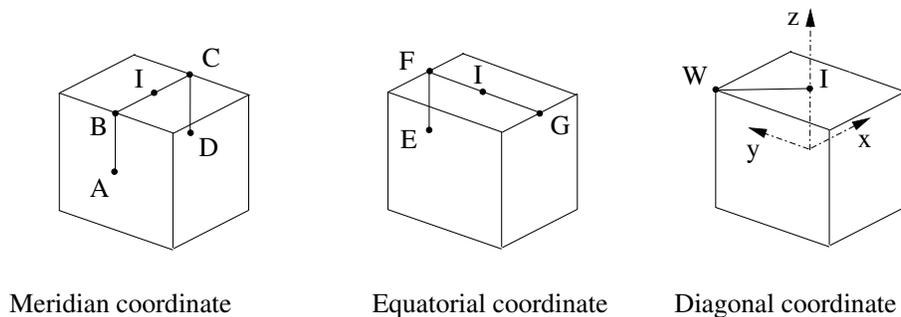
Figure 8: Meridian, equatorial and diagonal (polygonal) coordinates on the unit cube. The Cartesian coordinate system $O(x, y, z) = O(x_1, x_2, x_3)$ is centered.
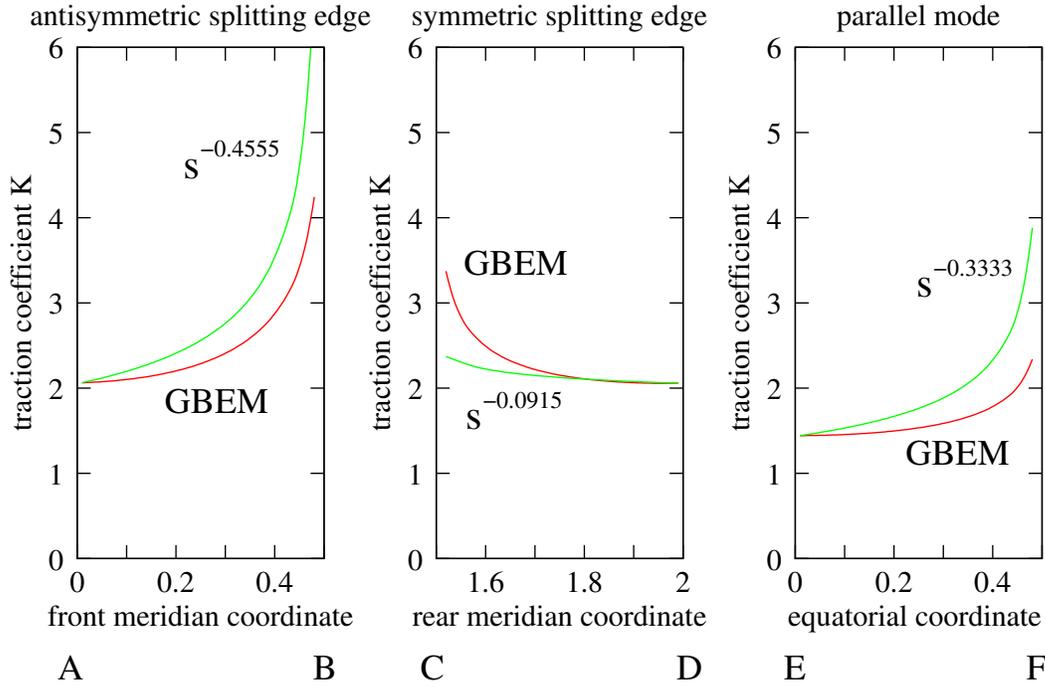
Figure 9: Quasi 2D steady creeping eigenmodes across the middle section of the unit cube: total traction coefficients K as a function of the coordinate: front meridian AB (left), rear meridian CD (center), and equatorial EF (right). GBEM computation (mesh 8, Table 1) and semi-analytical laws $O(s^p)$ (Mustakis and Kim, 1998), as a function of the distance s to the edge singularity.
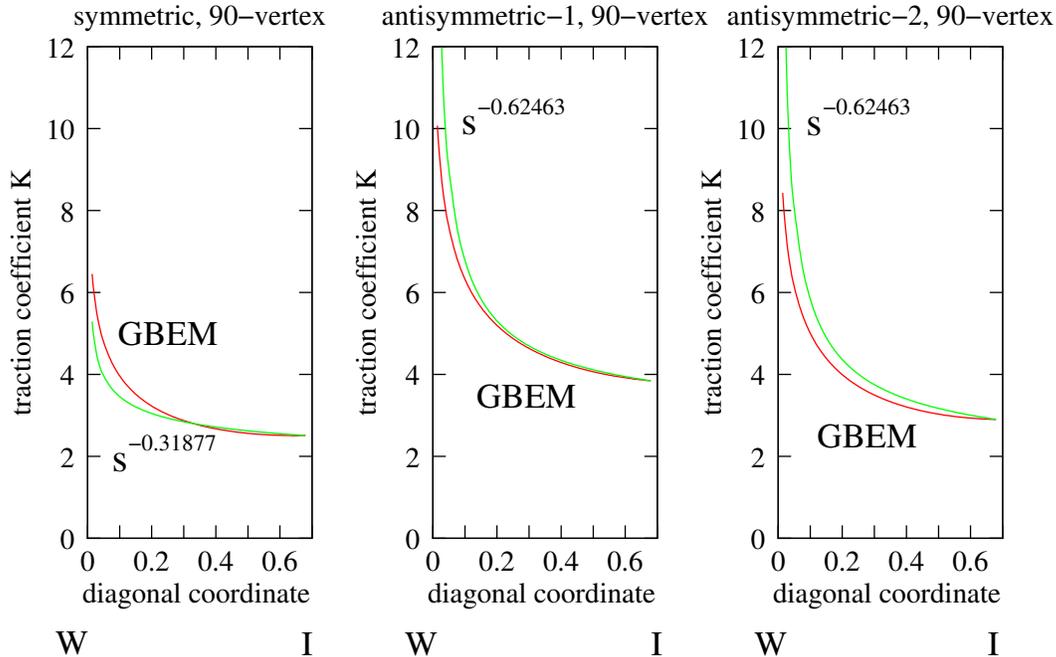
Figure 10: 3D steady creeping eingenmodes of the 90 degree vertex of the unit cube. Total traction coefficients K as a function of the coordinate along the diagonal WI on the top plane. GBEM computation (mesh 8, Table 1) and semi-analytical laws $O(s^p)$ (Mustakis and Kim, 1998), as a function of the distance s to the vertex singularity.
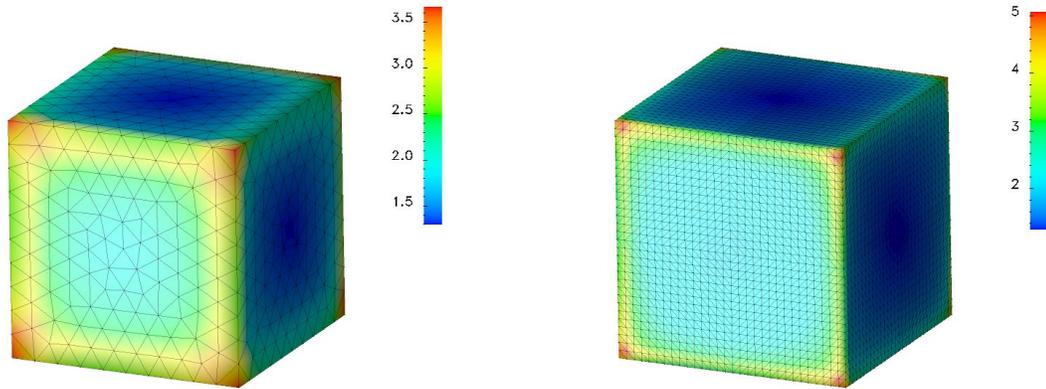
Figure 11: Colormaps of the τ_1 traction coefficient on the unit cube surface using a Q_{22} quadrature rule and meshes 12 and 10 (see Table 1) on left and right, respectively.
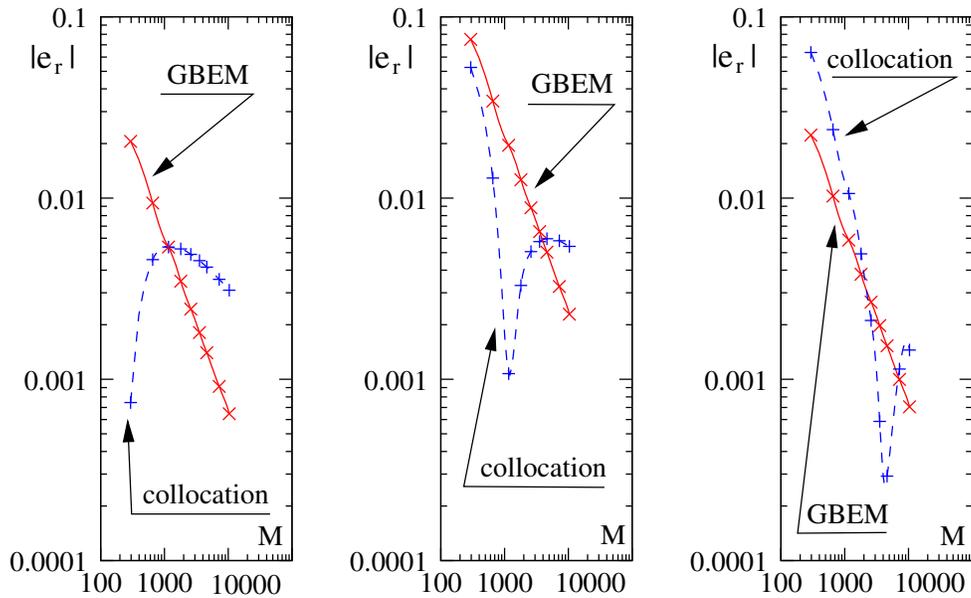
Figure 12: Absolute value of the relative error $|e_r|$ of the force coefficient K_i as function of the number of degrees of freedoms M on the unit sphere with smooth meshes and the Q_{22} quadrature rule. Galerkin (solid line) and collocation (dashed line): $e_r(K_1)$ uniform flow (left), $e_r(K_3)$ shear flow (middle) and $e_r(K_1)$ paraboloid flow (right).
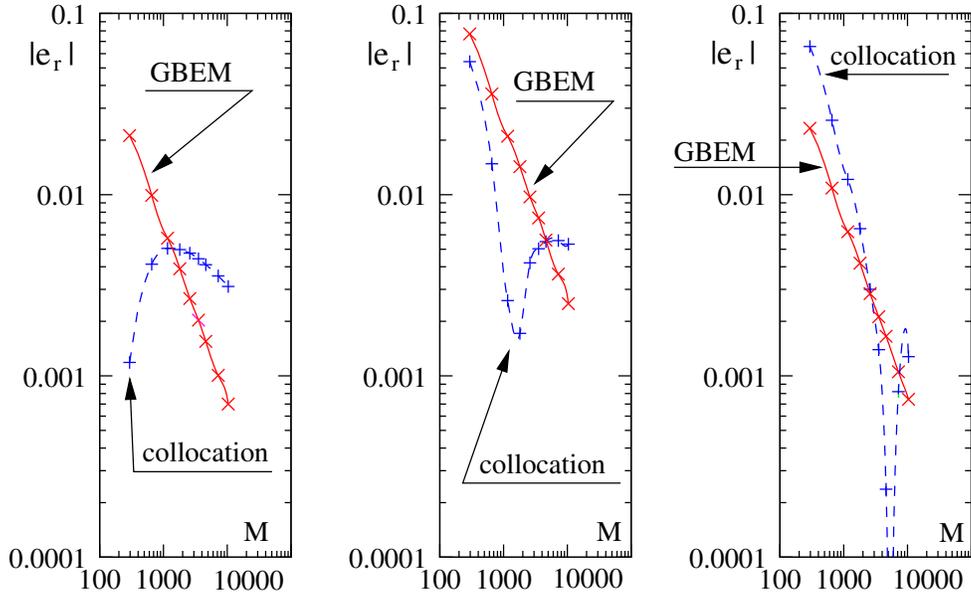
Figure 13: Idem Figure 12 with noisy meshes.
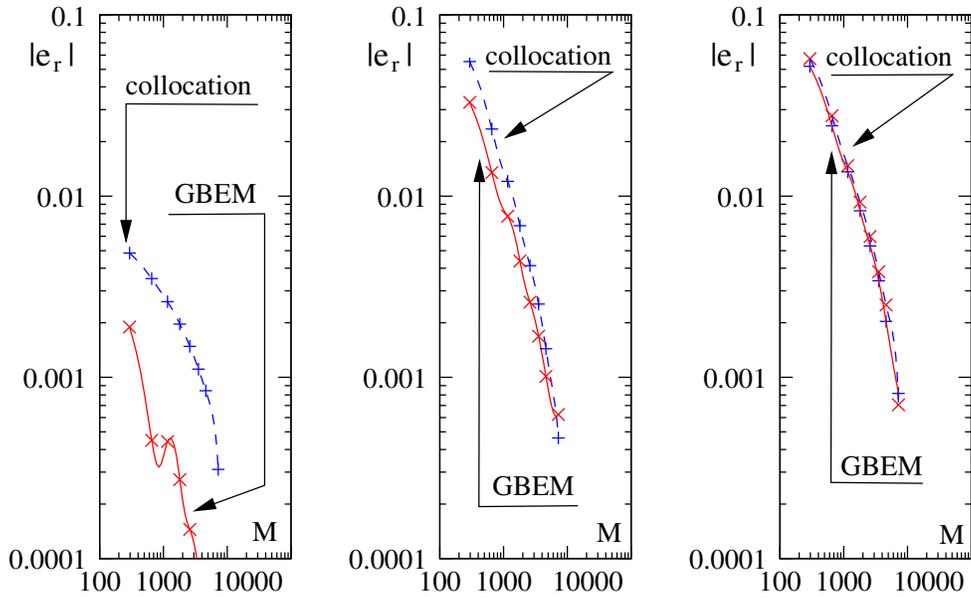
Figure 14: Absolute value of the relative error $|e_r|$ of the force coefficient K_i as function of the number of degrees of freedom M on the unit cube and the Q_{22} quadrature rule. Galerkin (solid line) and collocation (dashed line): K_1 uniform flow (left), K_3 shear flow (middle) and K_1 paraboloid flow (right).
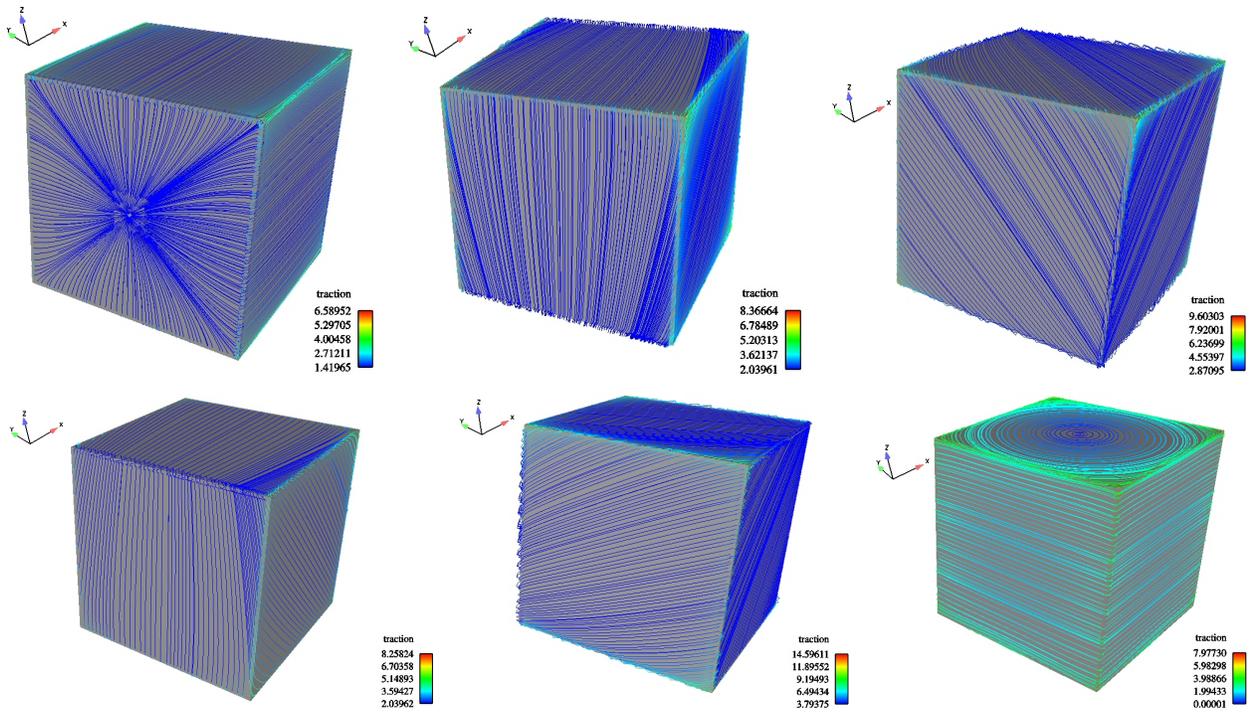
Figure 15: Surface friction line patterns of the velocity field close to the unit cube surface using a Q_{22} quadrature rule and mesh 8. At the top: parallel mode $\mathbf{U}_\infty = (1, 0, 0)$ (left), splitting mode $\mathbf{U}_\infty = (1, 0, 1)$ (center), symmetric mode $\mathbf{U}_\infty = (1, 1, 1)$ (right). At the bottom: antisymmetric I mode $\mathbf{U}_\infty = (1, 0, -1)$ (left), antisymmetric II mode $\mathbf{U}_\infty = (1, -2, 1)$ (center), and shear flow $\mathbf{U}_\infty = (x_2, -x_1, 0)/L$(right).
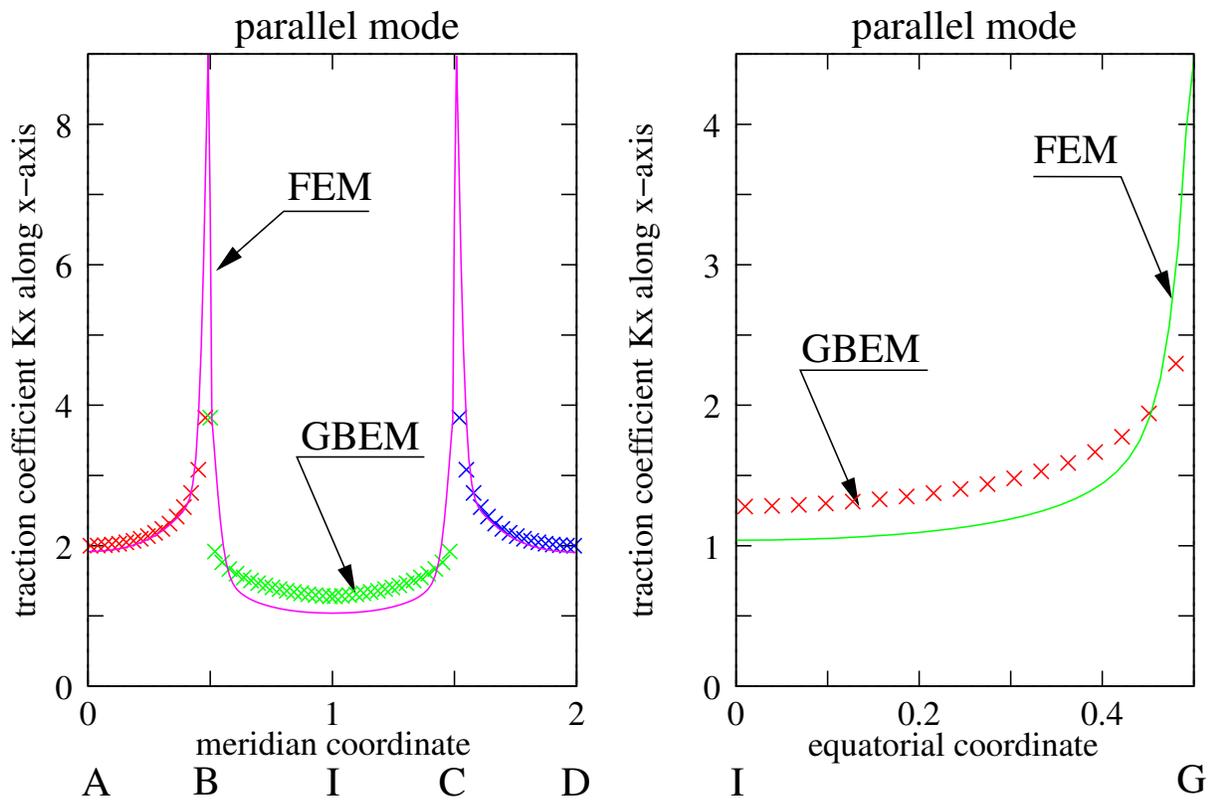
Figure 16: Cartesian K_1 component of the traction coefficient for the parallel mode $\mathbf{U} = (U, 0, 0)$ m/s, as a function of the meridional and equatorial (polygonal) coordinates s_m (left) and s_e (right), with FEM (solid line) and GBEM (crosses). See Fig. 8, left and center, for the position of the points $A - I$.